Physics – Uspekhi **58** (4) 345 – 364 (2015)

REVIEWS OF TOPICAL PROBLEMS

PACS numbers: **42.81. – i**, 87.19.L –, 87.85.D –

Neurophotonics: optical methods to study and control the brain

L V Doronina-Amitonova, I V Fedotov, A B Fedotov, K V Anokhin, A M Zheltikov

DOI: 10.3367/UFNe.0185.201504c.0371

Contents

1. Introduction **345**
2. Optical technologies in neurobiology **346**
2.1 Physical methods for the detection of neural activity in the living brain; 2.2 Optogenetics and fluorescent biomarkers; 2.3 Label-free optical methods for brain research
3. Fiber-optic technologies in neurophotonics **348**
3.1 Waveguide modes and light confinement in fiber-optic systems for neurophotonics; 3.2 Microstructured optical fibers; 3.3 Hollow-core photonic crystal fibers
4. Physical principles of fiber-optic neuroendoscopy **354**
5. Miniature microscopes for brain imaging in awake animals **357**
6. Fiber-optic neurointerfaces **357**
7. Multimodal optical brain microscopy **359**
7.1 Optical harmonic generation; 7.2 Spontaneous Raman scattering; 7.3 Coherent Raman scattering
8. Conclusion **362**
References **363**

Abstract. Methods of optical physics offer unique opportunities for the investigation of brain and higher nervous activity. The integration of cutting-edge laser technologies and advanced neurobiology opens a new cross-disciplinary area of natural sciences — neurophotonics — focusing on the development of a vast arsenal of tools for functional brain diagnostics, stimulation of individual neurons and neural networks, and the molecular engineering of brain cells aimed at the diagnosis and therapy of neurodegenerative and psychic diseases. Optical fibers help to confront the most challenging problems in brain research, including the analysis of molecular-cellular mechanisms of the formation of memory and behavior. New generation optical fibers provide new solutions for the development of fundamentally new, unique tools for neurophotonics and laser neuroengineering — fiber-optic neuroendoscopes and neurointerfaces. These instruments broaden research horizons when investigating the most complex brain functions, enabling a long-term multiplex detection of fluorescent protein markers, as well as photostimulation of neuronal activity in deep brain areas in living, freely moving animals with an unprecedented spatial resolution and minimal invasiveness. This emerging technology opens new horizons for understanding learning and long-term memory through experiments with living, freely moving mammals. Here, we present a brief review of this rapidly growing field of research.

Keywords: neurophotonics, fiber-optic probes, nonlinear optical microscopy

L V Doronina-Amitonova, I V Fedotov, A B Fedotov Lomonosov Moscow State University, Leninskie gory, 119991 Moscow, Russian Federation; Russian Quantum Center, ul. Novaya 100a, 143025 Skolkovo, Moscow, Russian Federation
K V Anokhin National Research Centre 'Kurchatov Institute', pl. Akademika Kurchatova 1, 123182 Moscow, Russian Federation
A M Zheltikov Lomonosov Moscow State University, Leninskie gory, 119991 Moscow, Russian Federation
E-mail: zheltikov@physics.msu.ru
Russian Quantum Center, ul. Novaya 100a, 143025 Skolkovo, Moscow, Russian Federation; National Research Centre 'Kurchatov Institute', pl. Akademika Kurchatova 1, 123182 Moscow, Russian Federation; Department of Physics and Astronomy, Texas A&M University, College Station, TX 77843, USA

Received 25 December 2014
Uspekhi Fizicheskikh Nauk **185** (4) 371 – 392 (2015)
DOI: 10.3367/UFNr.0185.201504c.0371
Translated by A M Zheltikov; edited by A Radzig

1. Introduction

Optical methods are finding growing applications in life sciences and biomedicine. Optical technologies are at the heart of highly informative schemes of brain research using fluorescent biomarkers [1, 2], chemically selective microscopy of spontaneous [3] and coherent [4, 5] Raman scattering, and high-spatial-resolution nonlinear optical microscopy based on two- and three-photon absorption [6–8], as well as second- and third-harmonic generation [9, 10].

Laser technologies offer unique opportunities for the solution of one of the central and most complex problems of neurobiology — identification and analysis of relations between the activity of neural cells and behavior of animals. Advanced methods of electrophysiology continue to play an important role in brain research, enabling the detection of activity of individual neural cells and leading to important discoveries in neurobiology, such as an identification of navigational place [11] and grid neurons [12], and head direction neurons [13]. These discoveries, shedding light on how the brain encodes the sense of place [14], were highlighted by the Nobel Prize for Physiology or Medicine 2014 [15].

Notably, the Nobel Prize for Chemistry 2014 was awarded to the inventors of ultrahigh-resolution fluorescence microscopy [16] — a technology that is finding rapidly growing applications in brain research.

Recently developed innovative optogenetic technologies [17], which employ genetically encoded light-sensitive ion channels and biomarkers, open the door to fundamentally new approaches to brain studies enabling a minimally invasive systematic investigation of large-scale distributed networks of electrically and chemically stimulated cells, including neurons and glial cells in the brain with the simultaneous monitoring of the behavioral and cognitive response of an animal in the course of a long-term experiment [18, 19]. Neurobiological studies of living, freely moving animals, which have become possible through optogenetic strategies [20], impose stringent requirements on the flexibility, compactness, mechanical durability, and functional universality of tools used to deliver and collect optical radiation in experiments of this class. In such studies, it is important to ensure an optimal geometry and high locality of neural stimulation, as well as to maximize the efficiency and minimize the loss in optical signal collection and delivery. A new generation of fiber-optic systems [21, 22] provides a unique platform for the creation of neurointerfaces for optogenetic experiments with living, freely moving animals, which meet all the above-specified requirements.

As will be shown below in this review, fiber-optic neurointerfaces help to confront the key neurobiological problem of studying deep brain layers in freely moving animals. Widely used methods of two-photon microscopy normally do not allow brain regions lying deeper than 1–1.5 mm to be interrogated [23], thus limiting studies to the cerebral cortex. Fiber-optic interfaces help to lift this limitation. Due to their compactness, mechanical flexibility, and high universality, fiber-optic neurointerfaces can enable minimally invasive optical diagnostics at an arbitrary depth inside the brain [24, 25]. This unique combination of properties makes fiber-optic neurointerfaces an indispensable instrument for neurobiological studies.

Here, we present an overview of fiber-optic systems for neurophotonics and discuss the most significant recent studies enabled by fiber-optic neurointerfaces. The outline of this review is as follows.

In Section 2, we examine the role of optical technologies in modern neurobiology. We will discuss physical methods for the detection of neural activity in the living brain and identify the key advantages of optical techniques in brain research. We will give a brief introduction to optogenetic technologies and consider methods of optical detection of neural activity using genetically encoded fluorescent biomarkers, as well as stainless, biomarker-free optical methods of brain studies, including technologies of nonlinear optical microscopy.

In Section 3, we shall deal with innovative fiber-optic technologies employed for the development of a fiber-optic platform for neurophotonics. We will briefly discuss the physical principles enabling fiber-optic neuroendoscopes and neurointerfaces and highlight the physics behind the confinement of electromagnetic fields in guided modes of ultrasmall-core waveguides. We will examine ways towards the creation of dedicated waveguide structures for neuroendoscopy with a high spatial resolution and review innovative fiber-optic systems and devices based on micro- and nanostructured fibers in the context of their growing applications in neuroendoscopes and neurointerfaces.

Section 4 is concerned with the physical principles of fiber-optic neuroendoscopy and new opportunities for studying the brain in freely moving animals with the aid of innovative fiber-optic neurointerfaces.

Section 5 analyzes novel approaches to studying the brain in freely moving animals, enabled by miniature portable microscopes that can be fixed to the head of an animal.

In Section 6, we overview studies aimed at the development of fiber-optic neurointerfaces.

Section 7 provides a brief analysis of the main physical processes enabling high-resolution fiber-optic endoscopy.

In the conclusion (Section 8), we summarize the main achievements in the development of fiber-optic systems for neurophotonics.

2. Optical technologies in neurobiology

2.1 Physical methods for the detection of neural activity in the living brain

Addressing the key problems of neurobiology — which deal with relations between the neural activity and behavioral tagging, adaptation, and learning — requires experimental tools that would enable studies of the variety of dynamic properties of neural circuits in live active animals with different types of cognitive response [26, 27]. Physical methods of brain studies, such as magnetic resonance imaging [28], positron emission tomography (PET) [29], and magnetoencephalography [30], help to take the first steps towards this goal. Each of these methods provides important information regarding the functional status of the brain. However, none of these techniques can ensure a spatial resolution necessary for studying the fundamental neurobiological processes underlying brain activity at the cellular level (Fig. 1). Despite successful PET studies of the brain of awake rodents [31], the above-listed techniques prove to be most efficient primarily in experiments on anesthetized and/or immobilized animals.

Electrophysiological methods still remain the main tool for studying the neural activity in live animals that are awake [32, 33]. The high sensitivity and high temporal resolution of

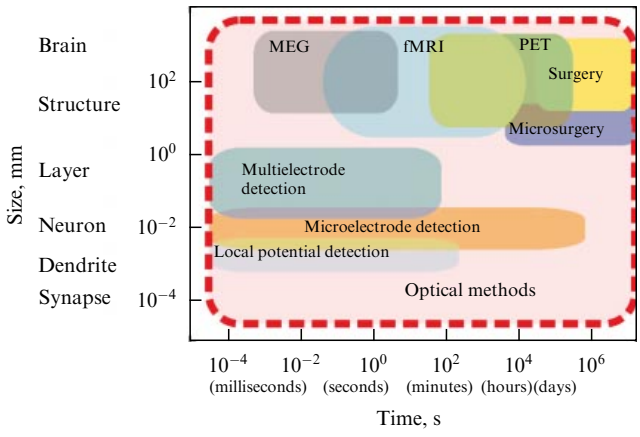

Figure 1. Physical methods for the detection of neural activity in the living brain and the role of optical technologies: positron-emission tomography (PET), functional magnetic resonance imaging (fMRI), and magnetoencephalography (MEG). The axes represent the spatial and temporal resolutions and show typical sizes of the most significant brain elements and structures. The applicability domain of optical methods is contoured with the dashed line.

advanced electrophysiological instruments are beneficial for detecting the response of individual ion channels and exploring the collective activity of several cells in a neural network. Direct detection of electrical signals induced by ion currents flowing through a cell membrane gives information on the state of neural cells without any proxy agents. As a flip side, direct electrical contact with a cell in electrophysiological studies may significantly influence its activity, distorting the result of measurements.

Optical methods can considerably reduce the unwanted effect of the probe on a cell and offer several fundamental advantages over other methods of brain studies. As one of their most significant benefits, optical technologies can enable a parallel detection of several factors of neural activities simultaneously. Optogenetic technologies, which have been developed within the past decade, employ genetically encoded light-sensitive ion membrane channels and fluorescent markers to allow specific classes of neurons to be activated or silenced using optical radiation, and enable studies of neural activity within a specific brain region through fluorescent signal detection [34]. Such an approach promotes detection of a broad variety of fundamental processes accompanying the activity of neural cells, including synapse formation, elimination and modification [35]. Fluorescent calcium indicators [36] and optogenetic markers [37] are successfully employed for the detection of calcium flows. Such probes permit the detection of electrical activity and variations in the membrane potential of a cell [38, 39] and help to analyze accumulation of proteins [40] involved in the processes of memory formation [41].

Rapidly progressing optogenetic technologies provide means to control the neural activity in freely moving animals with a high spatial and temporal resolution. To enable such experiments, targeted neurons are genetically encoded to express specific proteins, such as channelrhodopsin or halorhodopsine, playing the role of light-sensitive ion channels and allowing the stimulation or silencing of neurons [42–44]. Neurons expressing light-sensitive channels can be manipulated by optical radiation with the appropriate wavelength. This approach offers unique possibilities for studying neural activity and cognitive functions, helping to detect complex structural and functional changes in brain tissues, as well as to selectively control specific cells in a targeted brain region, thus providing means to probe their role in a certain neurobiological process [45].

To summarize, optical methods open new avenues in experimental studies of the brain, enabling a parallel detection of the electrical and genomic activity of neural cells through the use of voltage-sensitive dyes and specifically engineered markers. Optical technologies can be simultaneously instrumental in detecting the neural activity and dynamic changes within large brain areas with a high spatial resolution, thus providing a unique tool for studying the large-scale neural networks [46].

2.2 Optogenetics and fluorescent biomarkers

Advanced laser technologies enable optical microscopic studies of the brain with subcellular resolution, providing unique information on the anatomy, morphology, functional status, and pathologies of the brain. Optogenetic methods are used to label individual molecules, intracellular structures, and living cells with genetically encoded fluorescent markers. The protein marker systems usually consist of two parts — a protein, which undergoes structural changes sensitive to the parameters and processes under study (e.g., the membrane potential, intracellular ion flow dynamics, gene expression, protein accumulation), and a marker (usually a fluorescent protein), whose optical response is modulated by variations in the sensor protein (Fig. 2).

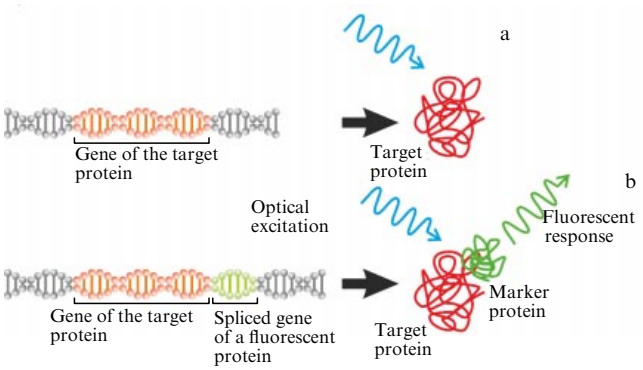

Figure 2. Genetic encoding of fluorescent protein markers: (a) a segment of a deoxyribonucleic acid (DNA) molecule encoding the targeted protein, and (b) a DNA segment with a built-in gene of a fluorescent protein. Expression of the gene of the target protein is accompanied by the expression of the gene of the fluorescent protein, enabling optical detection of the accumulation of the target protein in the brain region studied.

Extraction of the gene encoding green fluorescent protein (GFP) [47, 48] and subsequent synthesis of enhanced-fluorescence forms of this protein [49, 50] have opened a new phase in optogenetic brain studies. The main advantages of fluorescent protein biomarkers are due to the high stability of these proteins and their ability to form chromophores without cofactors, additional enzymes or agents other than molecular oxygen [49]. Importantly, GFP type markers are in most cases nontoxic for the targeted cells.

Thus, optogenetical technologies based on the optical detection of genetically encoded fluorescent proteins provide unique opportunities [51, 52] for the examination of neural activity and diagnostics of the functional state of the living brain in freely moving animals (Fig. 3).

2.3 Label-free optical methods for brain research

Synthetic or natural labels inevitably affect a variety of processes in a living biological system. In certain situations, such effects may distort the results of measurements, rendering fluorescent markers unwanted or even unacceptable. In particular, perturbations introduced by fluorescent markers are no longer negligible when measurements are performed on small molecules, such as indicator proteins, metabolites, neurotransmitters, or drug proteins whose sizes are less than the size of the protein marker. The use of markers is of particular concern in medical applications. As a consequence, optical methods allowing specific molecular signals to be detected without the use of markers attract much attention in the context of biomedical brain research [4].

The correlation between the functional activity of neural cells and their optical properties was revealed in the late 1940s [53], giving rise to a broad arsenal of label-free methods for brain diagnostics. One of the broadly used methodologies detects changes in the blood-vessel system sensitive to the functional state of the brain. The degree of blood oxygenation, related to the activity of neural cells, is one of the main parameters measured by such techniques [54]. Another

a

b

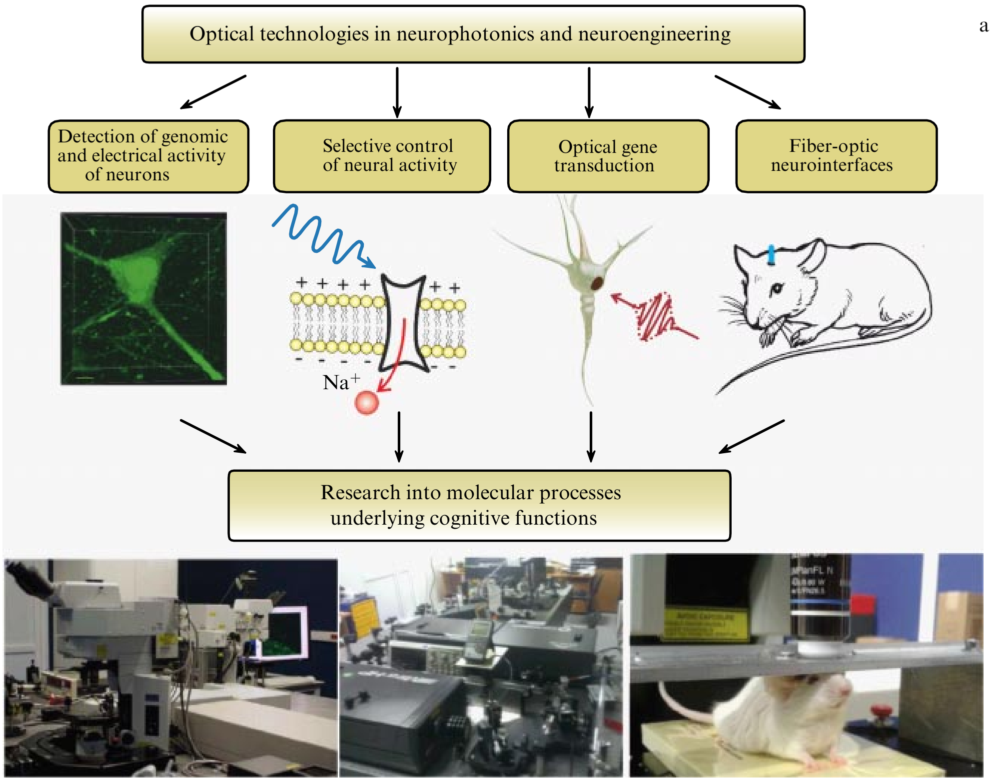

Figure 3. (a) Optical methods for studying and controling molecular and cellular mechanisms behind the cognitive functions. (b) Dedicated laser systems and microscopes developed for complex brain studies. The photographs are taken at the Laboratory of Neurophotonics of the Division of Neurosciences at the National Research Centre 'Kurchatov Institute' and the Laboratory of Photonics and Nonlinear Spectroscopy at Lomonosov Moscow State University.

important parameter, the volume of blood vessels, characterizes the incoming blood flow to brain tissues and is strongly correlated with the electrical activity of neurons in adjacent tissues [55]. Several efficient optical attenuation methods have been developed for measuring the dynamics of blood oxygenation [56]. The main limitations of the above-described techniques are due to the low spatial resolution and large time lag of variations in blood parameters in response to neural activity.

Nonlinear optical spectroscopy opens new avenues for label-free brain imaging and neural activity detection (Fig. 4). Nonlinear optical processes used for brain microscopy can be divided into two classes with regard to the coherence of the nonlinear signal utilized for imaging. Processes of the first type include multiphoton (two- and three-photon) absorption and stimulated emission depletion (STED) processes, including superresolving fluorescent STED microscopy. In these procedures, imaging is performed using an incoherent fluorescence signal. Nonlinear optical phenomena giving rise to a coherent signal fall into the second class of processes. This class includes second- and third-harmonic generation (SHG and THG), coherent anti-Stokes Raman scattering (CARS), and stimulated Raman scattering (SRS). The physical principles of fiber-optic endoscopy using nonlinear optical methods will be discussed in Section 7 of this review.

3. Fiber-optic technologies in neurophotonics

Experiments with living objects impose stringent requirements on optical instruments. Specifically, high reliability

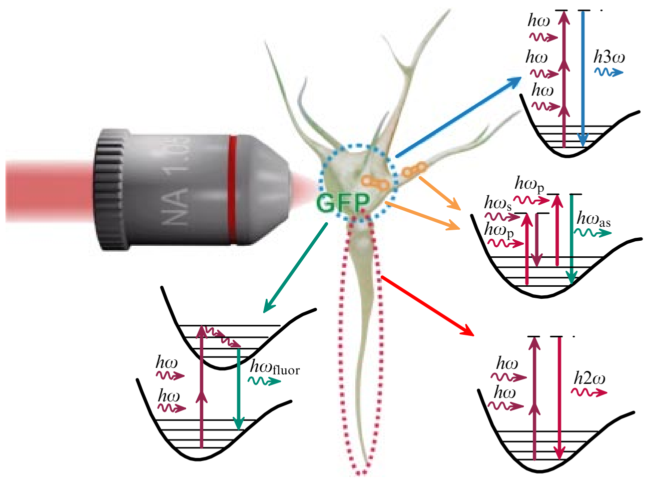

Figure 4. Multimodal nonlinear optical microscopy of the brain: quantum diagrams of second- and third-harmonic generation, coherent anti-Stokes Raman scattering, and two-photon-absorption-induced fluorescence.

and reproducibility of living brain studies on freely moving mice can only be achieved through an appropriate miniaturization of optical probes.

The central idea behind the miniaturization of optical microscopy [57], as illustrated in Fig. 5, is to separate an optical microscope from massive components of the setup, such as the laser sources, detection systems, and beam focusing and scanning controllers. Optical fibers are at the heart of the optical microscopy setup presented in Fig. 5.

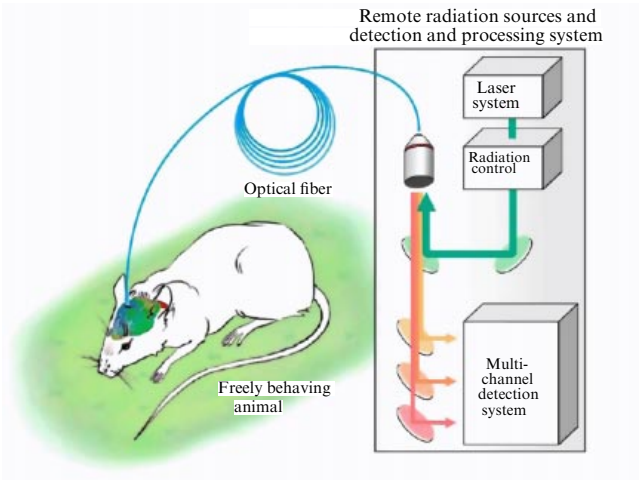

Figure 5. Miniaturization in optical neuroendoscopy. The key idea of this approach consists in physically separating the microscope components from massive elements comprising laser sources, the detection system, and the unit for automated control of focusing and scanning.

These fibers are employed to deliver laser radiation from the remote source to the region under study, collect the optical response, and guide the collected signal to the remote detector. Flexible and compact fiber-optic components allow measurements to be performed on freely moving animals.

The fiber-optic platform of neurophotonics makes wide use of innovative optical fibers, such as micro- and nanostructured optical waveguides. In Sections 3.1 to 3.3 of this review, we discuss the physics behind confinement of an electromagnetic field in waveguide modes of ultrasmall-core optical fibers, which hold much promise for neurophotonics, and consider new types of waveguide systems based on micro- and nanostructured optical fibers. These types of fibers are gaining growing applications as waveguide components for a new generation of neuroendoscopes and neurointerfaces.

3.1 Waveguide modes and light confinement in fiber-optic systems for neurophotonics

Developing subdiffraction microscopy techniques makes up one of the key trends in modern optical physics. Rapidly progressing methods of near-field microscopy [58] provide an unprecedentedly high spatial resolution of specific samples, giving access to unique information on the structure of matter and physical processes in subsurface layers.

Methods of near-field microscopy, however, face serious difficulties when applied to a broad class of problems related to studying processes and details of the structure in the bulk of a material and in living systems. Problems of this class can be attacked by using novel physical principles of far-field microscopy, such as multiphoton microscopy [59, 60], CARS and SRS microscopies [5, 61], and STED microscopy [62]. New methods of far-field microscopy have been shown to provide spatial resolution as high as a few dozen nanometers (in certain cases, better than 20 nm [63]). These techniques are finding widening applications in investigations of intracellular processes in living organisms, single-molecule detection, and analysis of a broad class of nanostructures and nanoobjects.

Modern fiber-optic technologies enable the creation of optical micro- and nanowaveguide systems, including sub-micrometer-core optical fibers [64]. Such components open vast opportunities for the implementation of novel methods of microscopy in the fiber format. The rapidly growing research in this field includes the development of fiber-optic sources and systems for the delivery of ultrashort light pulses for nonlinear optical endoscopy and the mapping of neuronal activity in the living brain [65, 66]. The unique possibilities offered by fiber-format ultrahigh-resolution microscopy call for a detailed understanding of fundamental physical factors controling the confinement of electromagnetic fields in waveguide systems and analysis of methods for transmission of ultracompact light beams in fiber-optic systems.

We consider a waveguide structure with an arbitrary transverse profile of the refractive index $n(r)$. The electric field of the waveguide mode supported by such a structure is written out as [67]

$$E(r,\varphi,z,t) = F(r)\cos(m\varphi)\exp(-\mathrm{i}\beta z)\exp(\mathrm{i}\omega t)\,, \qquad (1)$$

where z, r, and φ are the cylindrical coordinates, t is the time, $F(r)$ is the transverse field profile in the waveguide mode, m is the azimuthal mode index, β is the propagation constant, and ω is the radiation frequency.

The transverse field profile in the waveguide mode can be found by solving the relevant wave equation

$$\frac{\mathrm{d}^2F}{\mathrm{d}r^2}+\frac{1}{r}\frac{\mathrm{d}F}{\mathrm{d}r}+\left[\left(\frac{\omega}{c}n(r)\right)^2-\beta^2-\frac{m^2}{r^2}\right]F=0\,. \qquad (2)$$

The effective mode radius is defined as follows:

$$w=\left(\frac{S}{\pi}\right)^{1/2}, \qquad (3)$$

where

$$S=\frac{2\pi\left[\int_0^\infty |F(r)|^2 r\,\mathrm{d}r\right]^2}{\int_0^\infty |F(r)|^4 r\,\mathrm{d}r} \qquad (4)$$

is the effective mode area. We represent the transverse profile of the refractive index in the waveguide structure as

$$n(r)=\begin{cases} n_1\left[1-2\left(\dfrac{r}{\rho}\right)^g\Delta\right]^{1/2}, & 0\leqslant r\leqslant\rho\,,\\ n_2=n_1(1-2\Delta)^{1/2}, & \rho\leqslant r\,,\end{cases} \qquad (5)$$

where n_1 and n_2 are the refractive indices of the materials forming the waveguide structure, ρ is the core radius, and $\Delta=(n_1^2-n_2^2)/(2n_1^2)$. The exponent g in Eqn (5) controls the steepness of the refractive-index profile in the waveguide, with $g=1$ corresponding to a triangular profile of $n(r)$, and $g=2$ being a parabolic refractive-index profile. With very large g, one arrives at a step-index waveguide.

For a standard optical fiber, the mode radius can be quite accurately approximated with the Marcuse formula [68]

$$\frac{w}{\rho}\approx\frac{A}{V^{2/(2+g)}}+\frac{B}{V^{3/2}}+\frac{C}{V^6}\,, \qquad (6)$$

where

$$V=\frac{2\pi\rho}{\lambda}(n_1^2-n_2^2)^{1/2} \qquad (7)$$

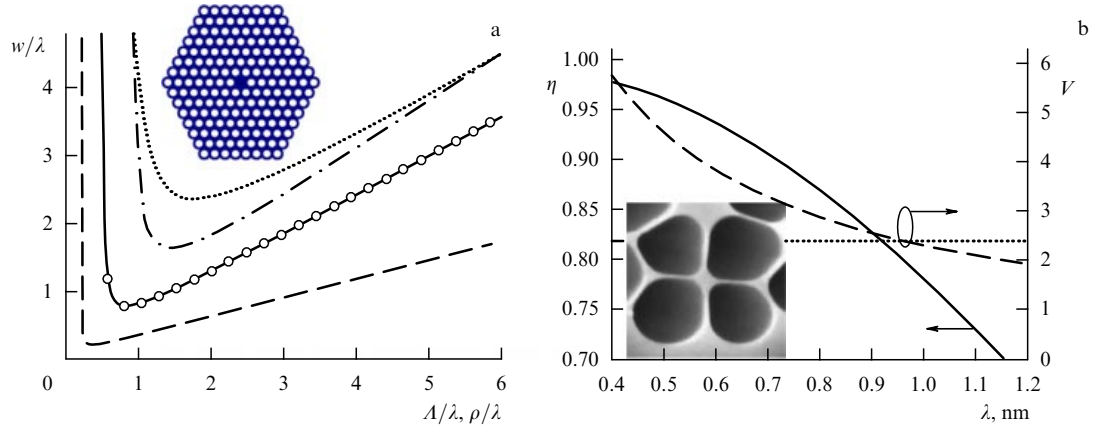

Figure 6. (a) Radius of the waveguide mode in a silica structured waveguide, calculated as a function of the lattice constant Λ using the approximation formula (9) for $\lambda = 1$ μm and $d/\Lambda = 0.3$ (dashed–dotted line), $d/\Lambda = 0.5$ (solid line), and $d/\Lambda = 0.9$ (dashed line). Unfilled circles show the results of a numerical solution of equation (2). The dotted line depicts the radius of the waveguide mode as a function of the core size ρ for a standard fiber with $n_1 - n_2 = 0.01$. The cross section of a photonic-crystal fiber is shown in the inset. (b) Parameter η characterizing the fraction of radiation power confined in the fiber core, and the waveguide parameter V as functions of the radiation wavelength for a silica waveguide channel with a radius of 350 nm (shown in the inset). The dotted straight line shows the boundary of the single-mode regime, $V = 2.405$.

is the waveguide parameter, λ is the radiation wavelength, and A, B, and C are numerical constants. For a step-index optical fiber, $g \to \infty$, the numerical constants in Eqn (6) take on the following values [68]: $A = 0.65$, $B = 1.619$, and $C = 2.879$.

The dotted line in Fig. 6a depicts the mode radius w normalized to the wavelength λ calculated as a function of the fiber core radius ρ for a standard weakly guiding optical fiber with $n_1 - n_2 = 0.01$. The waveguide parameter V quantifies the balance between diffraction and confinement of an optical beam due to total internal reflection in a waveguide structure. For large V, most of the power of the waveguide mode is localized in the fiber core. When V is low, on the other hand, a significant fraction of the mode power is guided in the evanescent part of the mode in the fiber cladding. These general properties of waveguide systems give important insights into the relation between the mode radius and the fiber-core size.

For fibers with a large core (high V), the electric field of a waveguide mode is tightly confined to the fiber core. In this regime, the mode size increases with the growth in the fiber core. For a step-index fiber ($g \to \infty$) with large V, the mode radius w, as can be seen from Eqn (6), scales linearly with the core radius (the dotted line in Fig. 6a): $w \approx A\rho$. For lower V, field confinement to the fiber core becomes weaker [67, 69]. As a consequence, for low V, a decrease in ρ leads to the growth in the mode radius (see the dotted line in Fig. 6a).

Let us consider now a waveguide with a cross-section structure typical of a photonic-crystal fiber (PCF) [70, 71] (see the inset to Fig. 6a). The central part of this waveguide, which serves as a waveguide core, is surrounded by a cladding that is built on a hexagonal lattice of air holes with diameter d arranged in a periodic structure with pitch Λ. For a fiber of this type, the waveguide parameter can be defined as [72]

$$V_{\mathrm{PCF}} = \frac{2\pi\Lambda}{\lambda}\left(n_1^2 - n_{\mathrm{eff}}^2\right)^{1/2}, \tag{8}$$

where n_{eff} is the effective refractive index of the structured cladding, which is defined as the effective index of the fundamental space-filling mode of an infinite ideal hexagonal lattice of air holes with diameter d separated by pitch Λ.

As shown by Nielsen et al. [72], with an appropriate choice of numerical constants ($A_{\mathrm{PCF}} = 0.7078$, $B_{\mathrm{PCF}} = 0.2997$, $C_{\mathrm{PCF}} = 0.0037$, and $g_{\mathrm{PCF}} = 8$), a modified Marcuse formula

$$\frac{w}{\Lambda} \approx \frac{A_{\mathrm{PCF}}}{V_{\mathrm{PCF}}^{2/(2+g_{\mathrm{PCF}})}} + \frac{B_{\mathrm{PCF}}}{V_{\mathrm{PCF}}^{3/2}} + \frac{C_{\mathrm{PCF}}}{V_{\mathrm{PCF}}^{6}} \tag{9}$$

provides an adequate accuracy of approximation to the ratio w/Λ as a function of V_{PCF}. Figure 6a compares calculated results for the mode radius as a function of the lattice constant Λ obtained with the use of Eqn (9) (solid line) and through a numerical solution of the wave equation (2) (unfilled circles). Within the considered range of parameters, predictions of approximate formula (9) deviate from the results of numerical simulations by less than 2%.

At a fixed d/Λ ratio, the waveguide parameter V_{PCF}, similarly to the V parameter of a standard fiber, provides a quantitative measure of the balance between diffraction and waveguide confinement of an optical beam. High V_{PCF} values correspond to a strong field confinement in the fiber core. In this regime, the mode radius increases with the growth in the lattice constant Λ. For low V_{PCF}, a decrease in Λ weakens field confinement in the fiber core. These tendencies give rise to a minimum in the dependence of the mode radius on the lattice constant Λ (Fig. 6a).

An increase in the ratio d/Λ lowers the effective refractive index n_{eff} of the PCF cladding, thus increasing V_{PCF} for a given value of Λ/λ. At sufficiently small d/Λ, the PCF can guide only one mode within the considered range of Λ/λ ratios ($V_{\mathrm{PCF}} < 2$ at $d/\Lambda = 0.3$). The minimum mode radius is then equal to $w_{\min} \approx 1.6\lambda$ (dashed–dotted line in Fig. 6a). In the case of large d/Λ, the field is tightly confined to the fiber core, even for small Λ/λ. In this regime, the minimum mode radius at $d/\Lambda = 0.9$ is achieved with $\Lambda \approx 0.37\lambda$ and is equal to $w_{\min} \approx 0.22$ (dashed line in Fig. 6a).

The strong field confinement to the core of a fiber with a large d/Λ ratio is due to the high numerical aperture of the waveguide structure. High-numerical-aperture fibers can efficiently collect the fluorescent response in fluorescence-based ultrahigh-resolution microscopy.

Several technologies are currently available for the fabrication of submicrometer-core waveguides. In fibers fabricated by means of PCF technologies, optical radiation can be guided along glass channels with a radius of less than 200 nm [73]. Such channels are usually surrounded by a cladding with a high content of air (see inset to Fig. 6b). High values of the index contrast Δ, typical of such waveguide systems, provide a strong confinement of the electromagnetic field in the glass channel [69, 74].

The silica waveguide structure shown in the inset to Fig. 6b is similar to a structure employed in experiments [73]. The radius of the waveguide channel in this structure amounts to 350 nm. Calculations presented in Fig. 6b suggest that such a waveguide is single-mode for wavelengths exceeding 970 nm (the boundary of the single-mode regime, $V = 2.405$, is shown by the dotted line). For the central wavelength of a Ti: sapphire laser ($\lambda = 800$ nm), the ratio of radiation power P_c confined in the silica channel to the total power P_0 of the guided mode (including the power of the evanescent part of the mode) is $\eta = P_c/P_0 \approx 0.87$ (the solid line in Fig. 6b). According to numerical simulations, the effective mode radius of radiation with a 800 nm wavelength is $w \approx 0.4\lambda$. This result agrees well with the experimental estimate for the nonlinearity coefficient of the waveguide structure:

$$\gamma = 2\pi\lambda^{-1} \int n_2(r)\, S_z^2\, \mathrm{d}^2 r \left| \int S_z\, \mathrm{d}^2 r \right|^{-2} \approx 400\ \mathrm{W}^{-1}\ \mathrm{km}^{-1},$$

where n_2 is the nonlinear refractive index, and $S_z = (\mathbf{E} \times \mathbf{H}^*)_z$ is the longitudinal component of the Poynting vector.

The technology of high-temperature microstructure-fiber tapering [75, 76] allows waveguide structures with a cross section as shown in the inset to Fig. 6a to be fabricated. Experiments on supercontinuum generation in such fibers indicate that the radiation field is localized in guided modes of such fibers within an effective mode radius of less than λ. In particular, for light pulses with a central wavelength of 800 nm, coefficients of optical nonlinearity indicating field localization within a waveguide mode with an effective radius $w \approx 0.4\lambda$ have been achieved.

Technologies of semiconductor nanoprocessing allow high-quality waveguides with a high numerical aperture to be fabricated. Such waveguides can localize the light field in waveguide modes with an effective mode area of less than 0.1 μm^2 [77], opening new avenues for optical signal processing [77–80] in the telecommunication range of wavelengths ($\lambda \approx 1.55$ μm). However, such waveguides cannot be used in the visible range because of the light absorption by silicon.

Thus, the wave-equation analysis of waveguide modes of micro- and nanowaveguide structures and examination of approximate solutions of this equation show that such waveguide structures can form and guide subwavelength optical beams. Field localization in the modes of such waveguides can be controlled by varying the structure of the waveguide. For dielectric optical waveguides with a periodic (photonic-crystal) cladding, our analysis revealed the existence of the optimal cladding lattice period that provides the highest field localization in the guided modes.

3.2 Microstructured optical fibers

The rapidly developing technology of microstructured optical fibers offers new solutions to the creation of fiber-optic neurointerfaces and neuroendoscopes. Optical fibers of this class, often referred to as photonic crystal fibers (PCFs), play an increasingly important role in optical physics as they find widening applications in modern optical devices and laser systems [70–79]. In their properties and guiding mechanisms, microstructured fibers significantly differ from standard optical fibers. Waveguide modes are confined in microstructured fibers within a solid (Fig. 7a) or hollow (Figs 7b, 7c) core surrounded by a microstructured cladding, where cylindrical air holes run along the fiber axis. Such a microstructure can be fabricated by drawing a preform consisting of capillary tubes and solid rods.

Along with standard, total-internal-reflection waveguiding regimes, microstructured fibers can guide radiation modes through unusual mechanisms. In hollow photonic crystal fibers, electromagnetic fields can be confined to the fiber core by a high reflectivity of a periodic fiber cladding within the photonic band gaps of this periodic structure [80–84]. Such waveguiding regimes exist in a hollow or solid core of fibers with a two-dimensional periodic microstructured (photonic-crystal) cladding. The photonic band gap in the transmission of such a structure provides a high reflectivity of the cladding, confining light to the hollow core and radically weakening the guidance loss, which would have been inevitable in the case of a conventional hollow fiber with a solid cladding, rapidly increasing with a decrease in the diameter of the hollow core.

Since the dispersion of microstructured fibers can be tailored by varying their structure [85–89], these fibers offer unique options for optical technologies and fiber laser systems. Microstructured fiber technologies help to implement complicated dispersion profiles that cannot be achieved for standard optical fibers. As a consequence, microstructured fibers enable the observation of new nonlinear optical

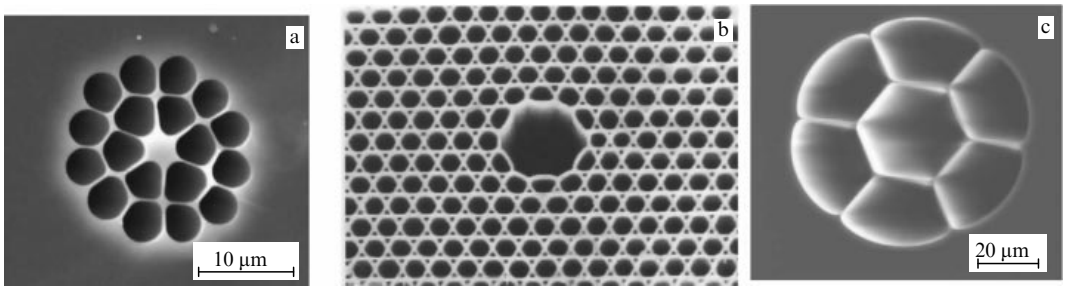

Figure 7. Scanning electron microscope images of cross sections of different types of microstructured fibers: (a) microstructured fiber with a high contrast refractive index step from the fiber core to the cladding; (b) hollow photonic crystal fiber guiding light due to the high reflectivity of the cladding within photonic band gaps, and (c) hollow antiresonance waveguide guiding light through a multibeam interference of waves reflected from the ring structure in the fiber cladding.

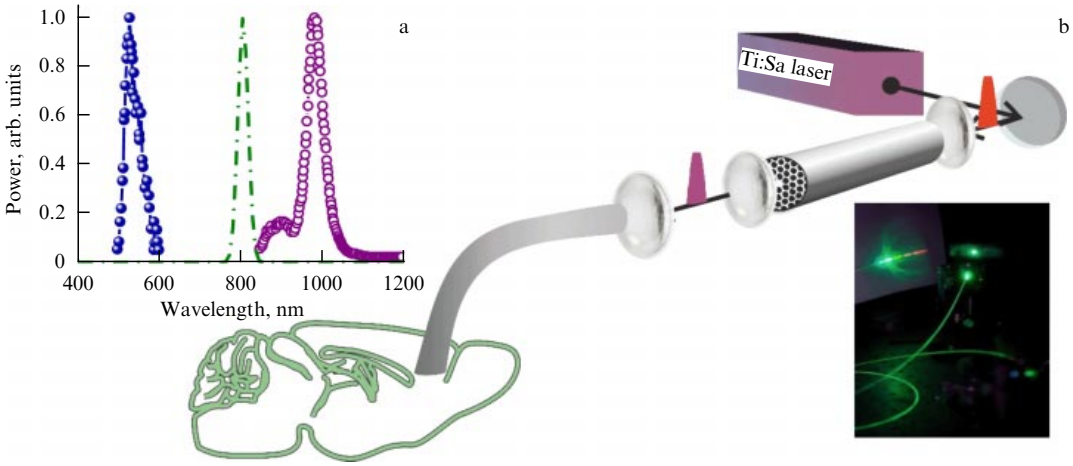

Figure 8. (a) Fluorescent response of Alexa Fluor 488 dye (filled circles) induced by the soliton output of a microstructured fiber (unfilled circles). The spectrum of the laser output is shown by the dashed–dotted line. (b) Diagram of an experiment on fiber-optic two-photon probing of fluorescent biomarkers using a frequency-tunable soliton output of a highly nonlinear microstructured fiber [66]. The soliton self-frequency shift in the microstructured fiber allows the spectrum of the soliton fiber output to be tuned to the maximum of two-photon absorption of the biomarker.

phenomena and unusual regimes of spectral and temporal transformations of ultrashort laser pulses [82].

Due to the high air-filling fraction of its cladding, a microstructured fiber with a cross-section structure, as shown in Fig. 7a, provides a high refractive index step from the fiber core to the fiber cladding. Strong localization of electromagnetic radiation in the core of such a fiber leads to high optical nonlinearity which translates into a high efficiency of nonlinear optical processes.

Highly efficient fiber-optic frequency converters of ultrashort pulses [82] and supercontinuum sources [86, 89] developed on a platform of highly nonlinear microstructured fibers help to solve fundamental problems in optical metrology [90, 91] and ultrafast optics [82]. Such components are finding extending applications in laser biomedicine [92] and nonlinear spectroscopy [93, 94] and microscopy [95, 96].

A soliton self-frequency shift in microstructured fibers enables the creation of wavelength-tunable sources of ultrashort pulses [97, 98]. Such fiber sources, as shown by Doronina et al. [66], can be helpful in maximizing the efficiency of two-photon excitation of fluorescent biomarkers in neurophysiological systems.

In the experimental setup shown in Fig. 8 [66], a microstructured fiber with dispersion and nonlinearity tailored for efficient and stable soliton frequency shifting provides a versatile source for the excitation of two-photon fluorescence of several biomarkers and helps to optimize the collection of this fluorescent response. The spectrum of the soliton output in such a fiber source can be tuned to match the maximum in the spectrum of two-photon absorption for a broad class of fluorescent biomarkers. Specifically, when pumped by femtosecond pulses from a Ti:sapphire laser with a central wavelength of 800 nm (the dashed–dotted line in Fig. 8a), the fiber shown in Fig. 8b generates a stable soliton at its output in the 980–990-nm wavelength range (unfilled circles in Fig. 8a). Such pulses are ideally suited for efficient two-photon excitation of enhanced green fluorescent protein (EGFP) or secondary antibodies conjugated with Alexa Fluor 488 dye, which find broad use as markers in cell biology and fluorescence microscopy. The two-photon-excited fluorescent response detected through the fiber probe [66] is plotted with filled circles in Fig. 8a.

Microstructured fibers substantially expand the functionality of fiber-optic systems, allowing several photonic components implementing different functions to be integrated into a single fiber [99]. Specifically, microstructured fibers with a dual cladding [100] offer much promise for the creation of innovative fiber sensors. In fiber lasers, dual-cladding microstructured fibers provide single-mode guidance with a large mode area, allowing the generation of high-energy laser radiation. In sensing components, the outer part of the fiber cladding is intended to provide a high aperture for efficient signal collection, and multimode guidance for low-loss delivery of the incoherent fluorescent response. Fibers of this class can be utilized to create optical sensors where coherent laser radiation is delivered through a small-diameter fiber core, thus providing local irradiation of an object under study and, hence, a high spatial resolution, while the outer part of the cladding serves to effectively collect the incoherent fluorescent response and deliver this signal in the opposite direction with reference to a detector [101–103].

3.3 Hollow-core photonic crystal fibers

Waveguide modes of hollow fibers differ in nature from the waveguide modes of standard fibers supported by total internal reflection. Since the refractive index of the core in hollow fibers is lower than that of the cladding, the modes localized in the core of such a fiber are leakage modes. For standard, capillary type hollow fibers with a thick solid cladding, the leakage loss of these modes scales as λ^2/a^3 [104] with the radiation wavelength λ and the core radius a. Because of this scaling, only capillary fibers with a large core diameter can be used in practice. Such fibers are inevitably multimode.

The technology of fabricating microstructured fibers helps to resolve the conflict between the guidance loss and the quality of the output beam profile for hollow fibers. In the most general form, the strategies of loss reduction and beam quality improvement in hollow fibers are based on optical antiresonance [105], or inhibiting the coupling between the modes confined in the fiber core and the cladding modes. Antiresonance effects can have a significant influence [108] on the mode properties of different types of microstructured fibers (see also review [105]). Antiresonant guidance in solid-

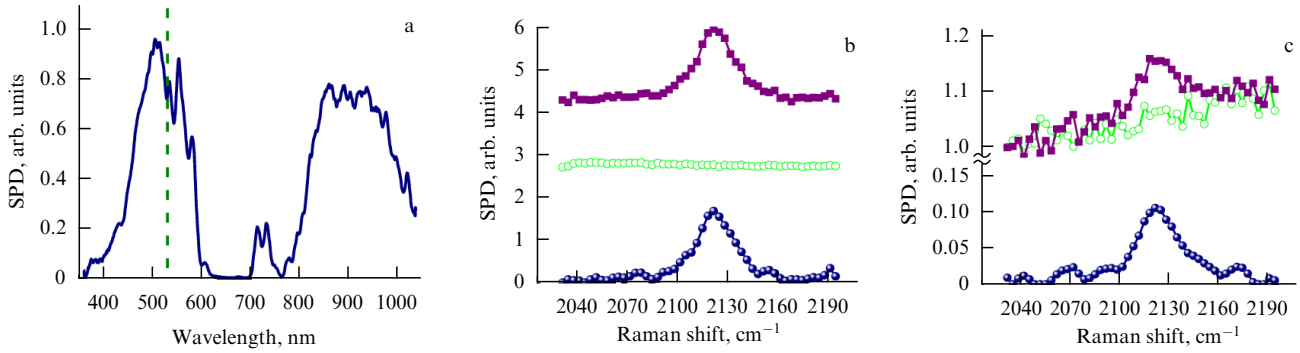

Figure 9. (a) Transmission spectrum of an antiresonance-guiding hollow-core fiber. The wavelength of a laser excitation radiation is marked by the dashed straight line. (b, c) The spectral power density (SPD) of the signal picked up by (b) a ring-cladding hollow fiber and (c) a standard index-guiding silica fiber: raw spectra from aqueous EdU solution (rectangles), the background signal due to Raman scattering in the fiber (unfilled circles), and spectra after background subtraction (filled circles) [111].

core microstructured fibers where the air holes of the cladding are filled with an analyte can be invoked for the creation of innovative fiber sensors [109].

Utilizing hollow-core fibers opens new avenues of inquiry for neurophotonics. Guidance of laser radiation through a hollow core not only allows optical studies of the gas medium filling the fiber core [110], but also helps to reduce or fully eliminate the optical background related to Raman scattering of laser radiation or luminescence of a fiber material. A properly engineered hollow fiber can thus radically improve the sensitivity of fiber probes for Raman sensing and imaging.

Antiresonance hollow fibers have been shown in paper [111] to be ideally suited as fiber-optic probes for brain studies taking advantage of spontaneous Raman scattering. In such probes, waveguide modes are confined in the air-filled fiber core due to the antiresonant reflection of radiation from the ring structure in the cladding. This ring structure plays the role of a built-in Fabry–Perot interferometer, giving rise to interference peaks and antiresonance dips [108, 112, 113], which translate into alternating minima and maxima in the optical transmission spectrum of the fiber. An image of a hollow antiresonance fiber is displayed in Fig. 7c.

The transmission band of antiresonance hollow fibers can be made much broader than a typical transmission window in the spectrum of a hollow-core photonic band gap fiber. Such a fiber (with a typical transmission spectrum as demonstrated in Fig. 9a) can deliver laser radiation and pick up the frequency-shifted Raman response without the need for an additional section of cladding or other guiding structures for reasons of the incoherent return. Unlike the cladding of photonic band gap fibers, which needs to form an extended photonic crystal, the cladding of antiresonance fibers can be made very compact, allowing such fibers to be assembled into fiber bundles for image transmission.

In a series of experiments [111], an antiresonance hollow fiber was employed to detect the Raman response of 5-ethynyl-2′-deoxyuridine (EdU), which are finding widening applications as a novel cell proliferation marker. The sensitivity of an antiresonance hollow fiber probe was compared with the sensitivity of a standard silica index-guiding fiber. The Raman lines related to the alkyne group and CH bonds of EdU, as well as the Raman band of water, were observed in the raw spectra of the signals collected with the aid of both the antiresonance hollow fiber and a standard index-guiding fiber. However, the difference in the properties of the background picked up by different types of fiber probes was striking (Figs 9b, 9c), thus indicating the difference in the physical origin of the background signal collected by these two fibers.

Indeed, the Raman signal emanating from the alkyne group of EdU and collected by the standard index-guiding fiber is observed against a strong background which strongly distorts the spectrum, dominating the signal on the wings of the alkyne-group Raman band (see rectangles in Fig. 9c). This background emission includes two main parts — an intense signal due to the Raman scattering inside the fiber probe, and a much less intense component due to the fluorescence from the EdU solution. For the subtraction of the background related to Raman scattering inside the fiber, the spectrum of this part of the background was measured in a separate experiment (see unfilled circles in Fig. 9c), where a 532-nm laser pump with an appropriate power was transmitted through the fiber probe in the absence of the Raman signal from the sample. The spectra measured with the use of a fiber probe based on the antiresonance-guiding hollow waveguide are strikingly different. Comparison of the overall background level in the raw Raman spectra measured with the use of the antiresonant hollow fiber probe (rectangles in Fig. 9b) with the background signal exclusively due to the Raman scattering in this fiber (unfilled circles in Fig. 9b) gives evidence that the background is dominated by broadband fluorescence from the EdU solution. As a result, the signal collected by the antiresonant hollow fiber probe is observed against a much less intense and much flatter radiation background.

To summarize, antiresonance-guiding hollow-core fibers enable highly sensitive detection of cell proliferation probes using Raman light scattering within the region where the cellular Raman activity is minimal. Experiments presented in this paper demonstrate that fibers of this class can substantially reduce the level of the background compared to standard index-guiding optical fibers, thus radically improving the sensitivity of Raman detection of DNA synthesis in cells and offering a powerful tool for fiber-based living-cell imaging [111].

Due to the strong wavelength dependence of the transmission of hollow-core PCFs, such fibers can be employed as fiber-format spectral filters. The advantages of such fiber filters have been demonstrated in experiments on a parallel all-fiber probing of several biomarkers [114]. A sketch of such an experiment is presented in Fig. 10a. Coherent broadband interrogation radiation was delivered (Fig. 10b) by means of

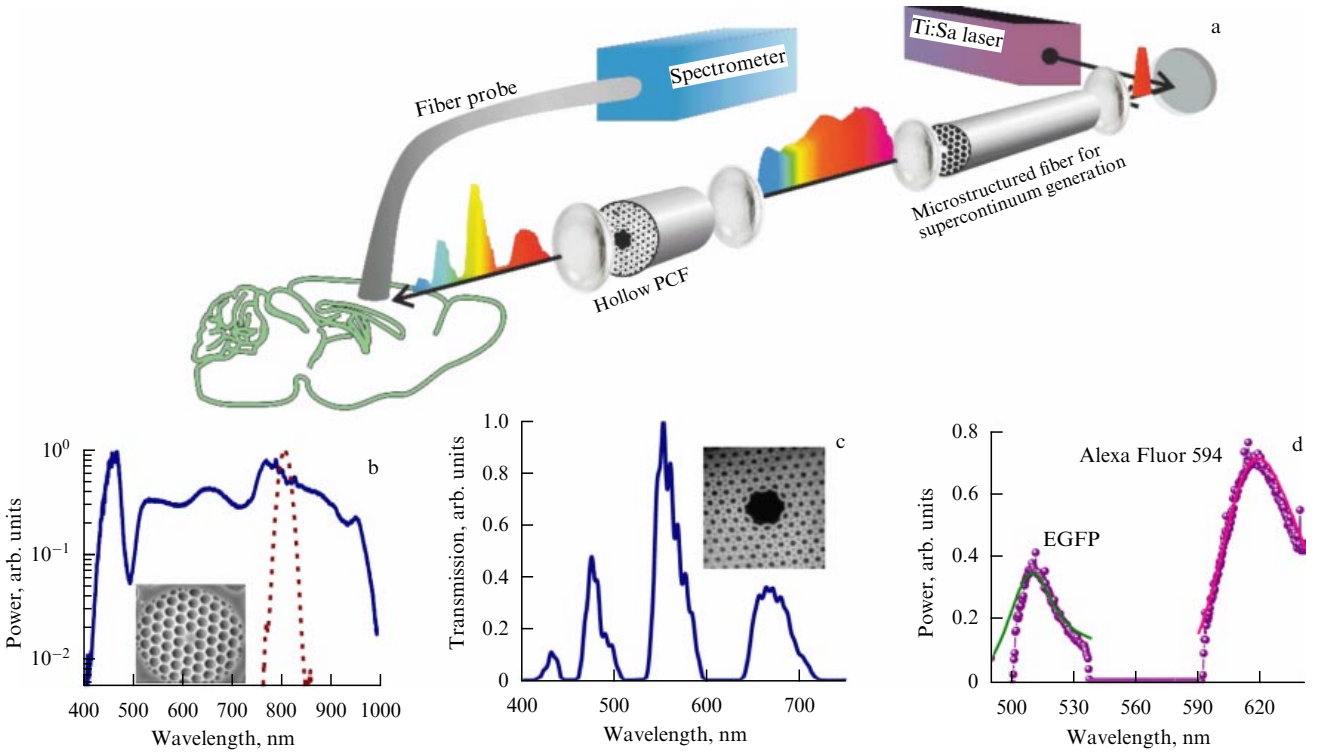

Figure 10. Diagram of fiber-optic excitation and collection of the fluorescence response from various markers in a mouse brain (a) using supercontinuum generation in a highly nonlinear microstructured fiber (b), and spectral filtering in a hollow PCF (c). Also shown are the spectra of EGFP and Alexa Fluor 594 fluorescent markers measured [114] with the aid of this fiber-optic system (d).

supercontinuum generation in a highly nonlinear microstructured fiber. The structure of this fiber is demonstrated in the inset to Fig. 10b. This fiber had a core diameter of 2 μm and zero group-velocity dispersion at a wavelength of 770 nm. A hollow-core PCF with a cross-section structure as shown in the inset to Fig. 10c served as a spectral filter. The structure of this PCF was designed in such a way as to guide only those parts of the supercontinuum spectrum that can efficiently induce the fluorescence of biomarkers in a mouse brain (Fig. 10c). Such a system has been shown to enable a simultaneous fiber-optic probing of several biomarkers in a mouse brain. The fluorescence spectra of EGFP and Alexa Fluor 594 biomarkers measured in this experimental setup are shown in Fig. 10d.

Hollow PCFs permit addressing several important issues inherent in a fiber-optic delivery of ultrashort laser pulses for the investigation and control of the brain.

First, the low optical nonlinearity of the gas filling the hollow fiber core helps to minimize unwanted nonlinear optical effects.

Second, low dispersion, typical of hollow PCFs away from the edges of the transmission band, minimizes the dispersion stretching of ultrashort light pulses.

Third, the laser breakdown threshold of a gas filling the hollow fiber core is several orders of magnitude higher than the laser breakdown threshold in a solid fiber core, which makes it possible to use higher laser intensities for brain studies, thus enabling the imaging of deeper brain domains.

Experimental studies demonstrate that hollow PCFs can offer attractive regimes of beam delivery for nanosecond [115], picosecond [116], and femtosecond [116] laser pulses fully compatible with biomedical applications. A broad class of biomedical applications call for optical systems capable of delivering femtosecond laser pulses, which can help to reduce both heat release and the rate of generation of reactive oxygen species, often causing the death of cells [117]. Strongly dispersive microstructured fibers may stretch femtosecond laser pulses, limiting applications of such fibers in a broad range of nonlinear optical biomedical technologies. This problem can, however, be addressed with an appropriate dispersion precompensation [118]. In particular, a hollow-core PCF with a core diameter of 15 μm has been used in paper [118] for a temporal compression of high-power femtosecond laser pulses (Fig. 11) to a pulse width of about 110 fs, yielding a peak power of about 5 MW.

4. Physical principles of fiber-optic neuroendoscopy

Correct interpretation of the results obtained with the aid of fiber-optic probes requires a clear understanding of the properties of excitation and collection of the fluorescence response by a fiber probe. A generic scheme of fiber-optic interrogation of biological tissues and collection of the fluorescence response is given in Fig. 12. The spatial resolution of such a method depends on both the parameters of the fiber probe and the optical properties of the medium under study. On the scheme considered, the fiber probe mostly interrogates a region adjacent to the fiber end. The volume of the interrogated region is determined by the volume of irradiated tissue and the specific geometry of signal collection.

All the key parameters of fiber-optic interrogation, including the sensitivity of the method and geometric sizes of the interrogated area, can be simulated by numerical methods using the following generic model. A fiber probe

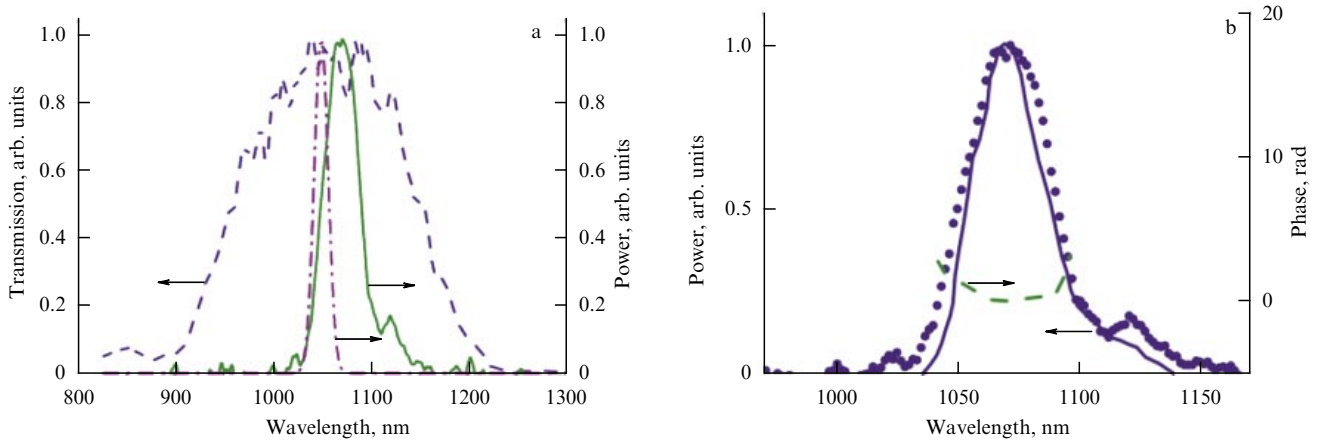

Figure 11. (a) Transmission spectrum of a hollow-core PCF (dashed line), the output spectrum of an ytterbium laser (dashed–dotted line), and the output spectrum of an optical parametric amplifier (solid line). (b) A typical laser pulse at the output of a hollow-core PCF: (circles) the measured spectrum, and (solid line) the spectrum and (dashed line) the spectral phase retrieved from cross-correlation frequency-resolved optical gating (XFROG) traces [118].

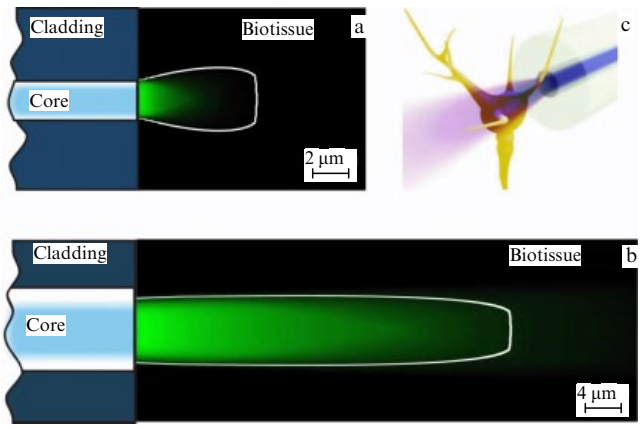

Figure 12. Fiber-optic probing of biological tissues. Maps of the $\psi(r,z)$ function calculated for a brain tissue with $n_0 = 1.36$ and $\mu_s \approx 11.3\ \text{mm}^{-1}$ and a fiber probe with (a) $a_{\text{core}} = 1$ μm and NA = 0.38, and (b) $a_{\text{core}} = 4.5$ μm and NA = 0.2. The contoured region provides 80% of the overall signal collected by the fiber probe. (c) Fiber-optic interrogation of individual neurons using small-core high-numerical-aperture fibers.

with a numerical aperture $\text{NA} = (n_{\text{core}}^2 - n_{\text{clad}}^2)^{1/2}$, where n_{core} and n_{clad} are the refractive indices of the fiber core and cladding, respectively, is assumed to deliver the interrogating radiation to a fluorophore-dye- or fluorescent-protein-doped tissue and collects the fluorescence response from the biotissue, capturing the fluorescence signal within the numerical-aperture-controlled acceptance angle $\theta_0 = \arcsin(\text{NA}/n_0)$, where n_0 is the refractive index of the tissue. The total power of the fluorescence signal collected by the fiber probe in such a scheme is given by

$$P \propto \sigma\eta N I_0 \int_0^\infty \mathrm{d}z \int_0^\infty \phi(r,z)\, f(r,z)\, T^2(r,z)\, r\, \mathrm{d}r\,, \qquad (10)$$

where σ is the absorption cross section, η is the fluorescence quantum yield, N is the density of fluorescent centers, which is assumed to be constant over the interrogated volume, r is the transverse coordinate measured from the axis of the fiber probe, z is the longitudinal coordinate measured from the output end of the fiber probe, and I_0 is the intensity of interrogating radiation in the center of the beam at the output end of the fiber probe, i.e., at $r = 0$ and $z = 0$. The function $\phi(r,z)$ defines the efficiency of fluorescence signal collection by the fiber probe at a give point. This function depends on the numerical aperture of the fiber, NA, and the full solid angle $\theta(r,z)$ of acceptance for the fiber:

$$\phi(r,z) = 2\pi \int_0^{\theta(r,z)} \sin\xi\, \mathrm{d}\xi\,.$$

The function $f(r,z)$ includes the divergence of the interrogating beam emerging from the output end of the fiber probe. The function $T(r,z)$ stands for the attenuation due to scattering and absorption. As is well known, the absorption length l_a in brain tissues is an order of magnitude larger than the scattering length l_s in the visible and near-infrared spectral ranges [119]. This allows us to neglect absorption and include only scattering effects without a loss of accuracy.

The function $\psi(r,z) = \phi(r,z)\, f(r,z)\, T^2(r,z)$ under the integral in formula (10) quantifies the contribution from a small volume inside the interrogated area centered at r and z to the total fluorescence signal collected by the fiber probe. Radiation attenuation due to scattering in a biological tissue can be calculated using a variety of approaches. The model adopted here leans upon the Kubelka–Munk model of diffuse scattering [120], according to which $T = T_{\text{KM}} = (\mu_s z + 1)^{-1}$, where $\mu_s = l_s^{-1}$ is the scattering coefficient, and l_s is the scattering length. For a multimode fiber, the function $f(r,z)$, which characterizes the divergence of the interrogating beam emerging from the output end of the fiber probe, can be represented in the following form:

$$f(r,z) = a_{\text{m}}^2 (z\tan\theta_{\text{d}} + a_{\text{m}})^{-2}\,,$$

where a_{m} is the effective fiber mode radius, and θ_{d} is the divergence angle of the interrogating beam emerging from the fiber. In the single-mode regime, the radial intensity profile in the beam emerging from the fiber can be approximated by a Gaussian function. With $f(r,z)$ written as $f(r,z) = a_{\text{m}}^2 (z\tan\theta_{\text{d}} + a_{\text{m}})^{-2}$ and using power-series expansions $f(r,z) \approx 1 - 2(z/a_{\text{m}})\tan\theta_{\text{d}}$ and $T_{\text{KM}} \approx 1 - \mu_s z$, valid for small z, we identify the characteristic pumping-

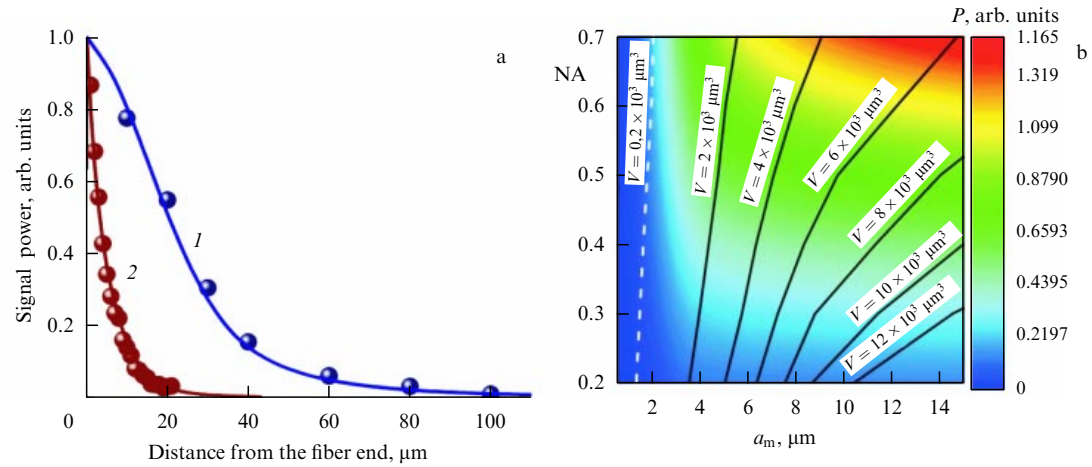

Figure 13. (a) Power of the fluorescence signal collected by the fiber probe from a fluorescent particle with a diameter of 6 μm as a function of the distance z from the fiber end for a standard fiber (curve *1*) and a microstructured fiber (curve *2*): (circles) experiments and (solid lines) calculations. (b) Power P of the fluorescence signal excited and collected by the fiber probe in a uniform fluorescent medium with refractive index $n_0 = 1.36$ as a function of the effective mode radius a_m and the numerical aperture NA for a constant excitation radiation intensity delivered by a fiber with $a_0 \approx a_m$ and $\theta_d \approx \theta_0$ [121]. The solid lines depict the isolines of a constant optical interrogation volume V provided by a fiber probe. The volume of a neuron body is marked by the dashed line.

beam-divergence length for a multimode fiber as $l_d \approx a_m/(2 \tan \theta_d)$.

Fibers with smaller cores and larger numerical apertures thus enhance the divergence of the interrogating beam, decreasing the volume interrogated by the fiber probe. Two physically different situations can be distinguished with regard to the relative significance of light scattering and diffraction effects. In the regime where $l_d > l_s$, the longitudinal dimension L of the interrogated region is controlled by scattering, while for $l_d < l_s$ the spatial scale L is determined by the diffraction of the beam emerging from the output end of the fiber probe.

Experiments and simulations show that the sizes of the region of efficient fluorescence-signal collection by a fiber probe with a flat output end are mainly determined by the fiber core diameter and the numerical aperture of the fiber, as well as the optical properties of the biotissue under study [121, 122]. In Fig. 13a, we compare the results of simulations and experiments performed for two types of optical fibers — a standard telecommunication fiber with a core radius of 4.5 μm (curve *1*), and a microstructured fiber with a core radius of 1 μm (curve *2*). The circles exhibit the power of the fluorescence response collected by the fiber, measured as a function of the distance between a fluorescent particle with a diameter of 6.5 μm, intended to model a nerve cell, and the fiber end. The fluorescence signal was collected by the same fiber. The theoretical model based on formula (10) is seen to provide an excellent fit for the experimental results for both fibers checked in experiments (cf. solid lines and experimental data points in Fig. 13a).

For a fiber with a core diameter of 50 μm and NA = 0.2, the volume of optical interrogation of a tissue with typical parameters of the brain (refractive index $n_0 = 1.36$ and scattering coefficient $\mu_s \approx 11.3$ mm^{-1}) is estimated as 10^5 μm^3. As the fiber core increases to 100 μm, this volume monotonically grows until the diffraction length l_d becomes comparable with the scattering length l_s. A further increase in the fiber core diameter does not lead to any noticeable growth of the interrogated region. The volume of this region is determined in this regime by the parameters of the tissue rather than the fiber parameters. Thus, fibers with a core diameter of about 50–100 μm help to collect and integrate the fluorescence response from whole brain structures.

When a standard single-mode fiber is utilized as a fiber probe, the volume of optical interrogation in a mouse brain tissue is estimated as 10^3 μm^3, which enables the detection of the fluorescence response from a few neurons. Results of simulations performed for a uniform fluorescent medium irradiated with a fiber probe with a core diameter of 9 μm are presented in Fig. 12b. The region of efficient signal collection provided by the fiber probe is shown in green. The white line depicts the region that provides 80% of the collected fluorescence response. Fiber probes of this type allow individual cells with a typical size of 7 μm (e.g., neurons) to be optically interrogated in a tissue with a density of cells at the level of $\rho \approx 2 \times 10^5$ cells per mm^3 (e.g., in the somatosensory cortex [123]). Indeed, the interrogated volume for this type of fiber probe, $V \approx 10^3$ μm^3, contains, on the average, less than one neuron for this type of brain tissue: $V < 1/\rho$.

Microstructured fibers with a small core diameter (2 μm or less) and a high numerical aperture (NA > 0.35) make it possible to probe regions with a volume of less than 100 μm^3, allowing fluorescence signal collection from individual neurons (the neuron volume is, on the average, estimated as 200 μm^3).

Methods of nonlinear optical microscopy can substantially enhance the locality of fiber-based optical interrogation [124]. With a properly optimized fiber probe, in particular, two-photon fluorescence microscopy has been shown to enhance the interrogation locality by more than two times compared to one-photon microscopy.

The natural trade-off between the locality of optical interrogation and the intensity of the fluorescence response, which eventually defines the sensitivity of optical interrogation, is illustrated in Fig. 13b, where the isolines of V are plotted against the map of the collected fluorescence signal power on the a_m – NA plane. The volume of a typical neuron body is marked by the dashed line. When a certain degree of locality is required, meaning that we need to stay on a certain V isoline in Fig. 13b, more intense fluorescence signals and, hence, higher sensitivities of optical interrogation can be

achieved by utilizing fiber probes with larger core sizes and higher numerical apertures. The key advantages of microstructured fibers for an optical interrogation of neurons can then be best appreciated by realizing that these fibers can combine a small core diameter with a high numerical aperture. In particular, small-core microstructured fiber probes ($a_{core} \approx a_m \approx 1$ μm, NA ≈ 0.4) confine optical interrogation domain to a volume of less than 50 μm^3. Such fiber-optic probes can provide access to individual neurons in brain regions with a high density of neurons and enable intracellular imaging.

Calculations show that the fluorescence response of a single neuron with a typical diameter of 7 μm in a biotissue with typical parameters of the brain, i.e., $n_0 = 1.36$ and $\mu_s = 11.3$ mm^{-1}, can be most efficiently collected by an optical fiber with NA = 0.7 and $a_0 = 2.5$ μm ($a_m = 2$ μm). With such a fiber, the power of the fluorescence signal collected from a cell adjacent to the fiber end is increased by an order of magnitude relative to the power of the fluorescence signal collected by the fiber probe providing the highest spatial resolution.

Bundles of closely spaced optical fibers offer a convenient way of fiber-optic endoscopy and imaging. Each fiber in such a bundle provides an efficient collection of fluorescence signal from its own volume of interrogation. Each such interrogated volume is then represented by a single pixel of the image synthesized by the fiber bundle. The spatial resolution of such an image is determined by the above-discussed parameters of individual fibers in the bundle and the distance between these fibers. The volume interrogated by an individual fiber in the bundle defines the physical size of the pixel, while the distance between the fibers determines the distance between the pixels. According to simulations performed with the application of the above-described model, an optimal trade-off between the sensitivity and locality of fiber-optic brain interrogation is achieved with a fiber core diameter of about 2.5 μm. A bundle of such fibers makes possible an interrogation of neural activity in a mouse brain with maximum sensitivity and cellular resolution.

5. Miniature microscopes for brain imaging in awake animals

Considerable progress in experimental studies of the brain in living animals has been achieved thanks to ultraminiature portable microscopes that can be fixed directly on the head of a freely moving animal. The key elements of such a microscope comprise a single-mode fiber, which delivers femtosecond laser pulses to the brain region under study, a miniature scanner, optical imaging components, an objective, dichroic mirrors, and a photoelectric multiplier. Dispersion of a single-mode fiber is compensated by specifically designed dispersive gratings. The first generation of such miniature microscopes provided a subcellular spatial resolution at a depth of up to 250 μm inside the brain of anesthetized rats [125].

Flusberg et al. [126] have demonstrated a miniature microscope built around a hollow-core photonic-crystal fiber. Such a fiber can provide a high-throughput delivery of femtosecond laser pulses without dispersion precompensation. Its small weight (3.9 g) enables studies of anesthetized mice. Göbel et al. [127] have implemented a two-photon microscope with a fiber bundle and a gradient lens at its output end. A dual-cladding photonic-crystal fiber has been shown to provide a high-throughput delivery of laser radiation and highly efficient signal collection in brain mapping experiments [101].

A new generation of miniature fiber-optic microscopes enables studying animals that are awake with a high spatial resolution [128]. These devices have been designed to demonstrate brain imaging in freely moving animals with a subcellular resolution at a depth of up to 250 μm. The weight of such a microscope can be reduced to 2.9 g [129, 130].

Much effort in recent years has been focused on the development of light (1–2 g) miniature microscopes for one-photon fluorescence imaging. Flusberg et al. [65] have demonstrated a 1.1-g miniature module for high-speed one-photon microscopy. The tapping of ultracompact photodiodes and a high-speed camera enabled the creation of compact fiber-free miniature microscopes providing spatial resolution at a level of 2.5 μm [131].

Miniature microscopes fixed to the head of an animal have helped in performing several important experiments, including the analysis of dynamic changes in neural circuits consisting of navigational place cells [132]. Investigations of relations between the neural activity and behavioral taggings require long-term measurements on a single animal. To address this problem, a special technique for the implantation of gradient lenses has been developed [133]. Currently, much effort is bent to the development of miniature microscopes for clinical applications [134–138].

6. Fiber-optic neurointerfaces

Strong scattering of laser radiation in brain tissues, leading to its small penetration depths, is one of the main limitations of optical brain imaging. For standard parameters of laser pulses applied in brain imaging (average power of 1 W, repetition rate of 80 MHz, and pulse width of 100 fs), the penetration depth in the cerebral cortex ranges from 500 to 700 μm. At largest penetration depths in this range, the spatial resolution is not sufficient to image neurons, so that only a system of vessels (at a depth of about 600 μm) or glial cells (up to 700 μm) can be imaged.

Several methods have been proposed to increase the imaging depth in the optical microscopy of the living brain. The use of regenerative amplified laser pulses allows two-photon brain imaging to be extended to penetration depths of up to 1000 μm [141, 142]. At higher peak powers of laser radiation, however, the risk of tissue photodamage substantially increases [117]. Alternatively, the radiation wavelength can be increased. The supply of femtosecond pulses of a Cr:Forsterite laser at a central wavelength of 1280 nm has been shown to pave the way to brain imaging at depths exceeding 1000 μm [143]. A high-power tunable PCF-rod source delivering laser pulses with a central wavelength of 1700 nm has been shown to originate the three-photon fluorescence microscopy [8]. At this wavelength, an optimal trade-off between scattering and absorption of laser radiation in brain tissues is achieved. However, this approach does not allow imaging of brain regions lying deeper than 1.2 mm and employs a fixed radiation wavelength, restricting this methodology to a limited range of fluorescent markers.

Fiber-optic systems for the delivery of laser radiation and collection of fluorescence signals can help to overcome the difficulties of optical methods related to the strong scattering of laser radiation in brain tissues. In Fig. 14a, we present the response of enhanced green fluorescent protein (EGFP)

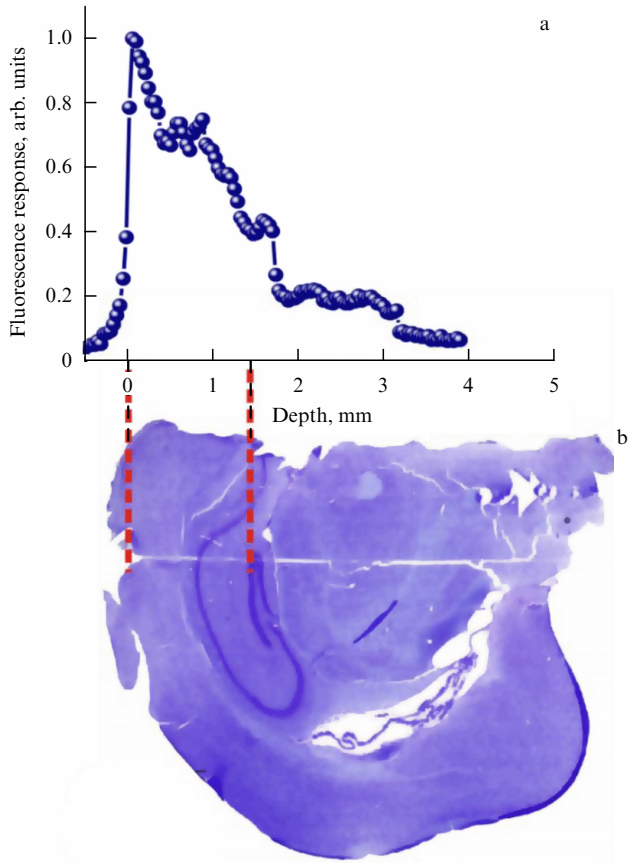

Figure 14. (a) Intensity of the fluorescence response of enhanced green fluorescent protein measured as a function of the depth inside the brain of a living zif-EGFP transgenic mouse. The fluorescence response was excited and collected with the same optical fiber. (b) Map of the mouse brain obtained applying the *in vitro* Nissl staining method.

measured with the aid of a fiber-optic probe in the brain of a living transgenic zif-EGFP mouse [144]. A fiber probe with a core diameter of 9 μm and an outer diameter of 125 μm carried out scanning with a step of 40 μm. This scanning step was sufficient to detect typical activity patterns in different regions of brain. Importantly, the damage to living brain tissues from a single scan of a 125-μm-outer-diameter fiber probe is so insignificant that the track from this scan is not even visible in Nissl-staining brain images. The track from the fiber probe becomes visible (Fig. 14b) only after performing more than ten scans.

Important information on deep brain regions can be obtained by employing bundles of optical fibers (Fig. 15). This technology enables the detection of the neuron calcium activity in the dentate gyrus part of the hippocampus at a depth of 3.4 mm from the cortex, and of thalamus nuclei at a depth of 5.6 mm from the cortex with a VARTA-1 Oregon green dye used as a marker [145]. Fiber bundles have also been shown to allow *in vivo* studies of gene expression [146] and neuroblast migration in the frontal part of the brain [147], as well as a multicolor imaging of subcortical layers in the brain of living mice labelled with three different markers [148]. With an appropriate choice of the size of fibers and the distance between individual fibers in the bundle, this technique has been demonstrated to provide a spatial resolution comparable with the resolution attainable in a standard *in vitro* confocal microscopy.

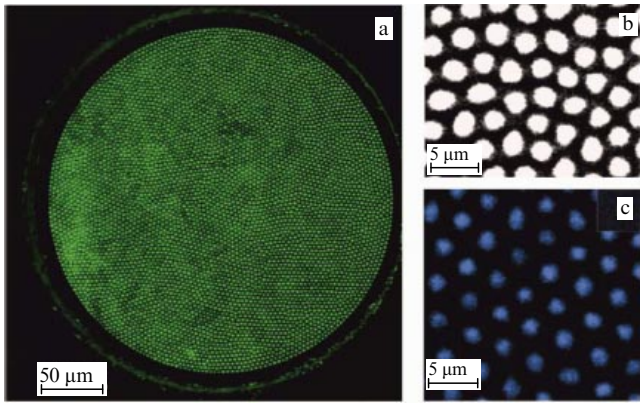

Figure 15. Photograph of a fiber-bundle probe end used for endoscopic brain imaging: (a) a panoramic image, and (b, c) a zoom-in on parts of the fiber bundle. An individual fiber in the bundle has a diameter of about 2.4 μm (b). The diameter of the waveguide mode supported by an individual fiber in the bundle at a wavelength of 473 nm is about 1.4 μm (c).

Figure 16 presents images of neurons [148] in the dentate gyrus part of the hippocampus in a Thy1-EGFP transgenic mouse additionally labelled with a DAPI dilactate marker which helps to image the cell bodies (blue in Fig. 16). The cells expressing Thy1-EGFP are seen colored green [148].

Fiber-optic endoscopes are successfully applied for the detection of neural activity in deep brain layers in freely moving mice [144, 149, 150]. Due to a small weight and size of the fiber probes, experiments can be performed within a period of several days [149]. Longer experiments, however, meet with difficulties, as rodents tend to damage the implanted fiber. As a result, the mice have to be kept in special conditions for long-term experiments outside their natural environment, which may influence their behavior tagging and lead to systematic errors in behavioral studies.

These problems can be addressed with the use of specifically designed fiber-optic neurointerfaces. Such interfaces have been shown to enable the long-term (within a month) detection of zif268 transcription factor gene expression in the cortex and hippocampus in freely moving mice [22, 151]. A fiber-optic interface developed for such measurements consists of an implantable module, which is fixed on the head of a mouse, and a measurement fiber, which is connected to the implantable module during measurement. Due to the

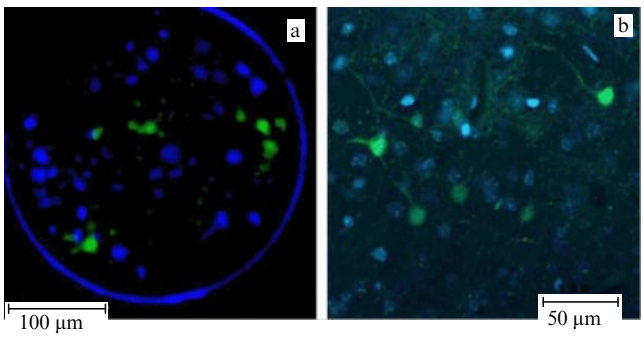

Figure 16. (Color online.) Two-color images of dentate gyrus in the hippocampus of transgenic Thy1-EGFP mice additionally stained with DAPI dilactate acquired in a living mouse with the aid of a fiber-bundle microprobe (a) and with fixed brain slices from the same mouse by means of confocal microscopy using the Olympus FluoView 10 system (b).

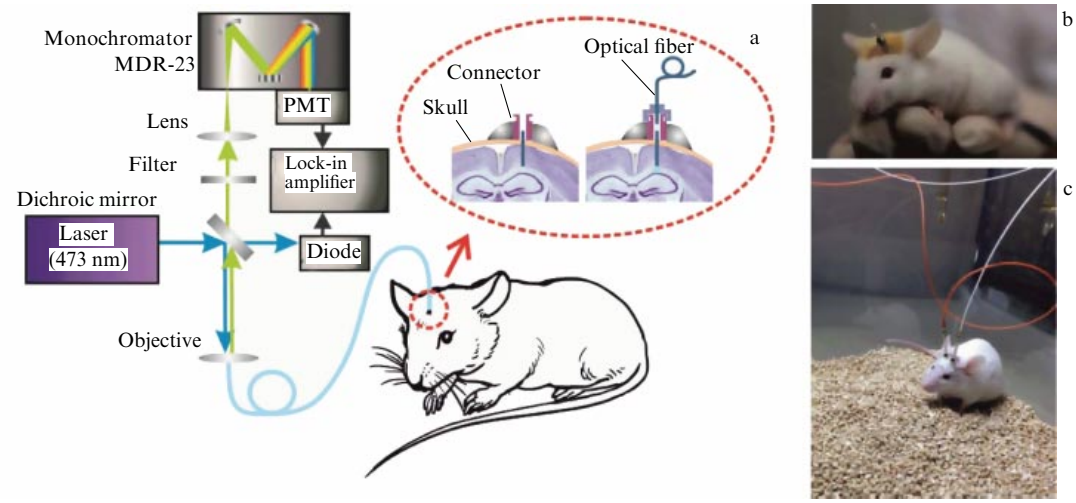

Figure 17. (a) Long-term interrogation of neural activity in deep brain layers in a freely moving animal using a two-section fiber-optic neurointerface. Also shown are photographs of mice used in experiments with an implanted module of the fiber-optic neurointerface with the longer part of the neurointerface employed for measurements disconnected from (b) and connected to (c) the implanted module.

small weight and sizes of the implantable module, consisting of a fiber-optic connector and a stretch of fiber implanted in the brain region under study, the mice are kept in standard cages in a normal environment all the time between measurements.

Figure 17a presents a sketch of a long-term optical interrogation of neural activity in deep brain regions of a freely moving mouse with the aid of the developed fiber-optic neurointerface. Measurements are performed by connecting a fiber of the required length, coupled to a laser source, to the implantable part of the fiber-optic neurointerface. Photographs of mice with implanted fiber-optic interfaces are displayed in Fig. 17b [22].

Thus, fiber-optic neurointerfaces make it possible to confront one of the long-standing challenges in neurophotonics by implementing a parallel optical detection of neural activity and interrogation of the functional state of the brain simultaneously in several spatially separated brain domains in freely moving animals [22].

7. Multimodal optical brain microscopy

7.1 Optical harmonic generation

Methods of nonlinear optical microscopy based on second- and third-harmonic generation enable stainless studies of biotissues without fluorescent markers [9, 152]. The efficiency of third-harmonic generation (THG) is controlled by the third-order nonlinear-optical susceptibility $\chi^{(3)}$ and the mismatch between the phase φ_h of the third-harmonic field and the phase φ_p of the nonlinear polarization induced in the medium by the laser driver. The phase mismatch $\Delta\varphi = \varphi_h - \varphi_p$ can be represented as a sum of two terms [153]: $\Delta\varphi = \Delta\varphi_m + \Delta\varphi_g$, where $\Delta\varphi_m = \Delta kz$ is the phase mismatch due to the dispersion of a medium, $\Delta k = 6\pi\Delta n/\lambda_p$, where λ_p is the wavelength of the laser pump, Δn is the difference between the refractive indices of the medium at the frequencies of the pump and the third harmonic, z is the coordinate along the beam, $\Delta\varphi_g = 4\arctan(z/b)$, $b = 2\pi n w_0^2/\lambda_p$ is the confocal parameter, n is the refractive index, and w_0 is the beam waist radius.

Phase-matching effects play an important role in third-harmonic generation. It is well known from the theory of nonlinear optical interactions that third-harmonic generation in tightly focused beams is prohibited in an optically uniform extended medium. However, optical inhomogeneities near the focus of a tightly focused laser beam (see the inset to Fig. 18a) remove this prohibition. As a consequence, third-harmonic generation can help to detect hidden interfaces, optical inhomogeneities, and voids [9, 152]. The third-harmonic efficiency is especially high when the size of an optical inhomogeneity is close to the confocal parameter of the driver beam: $b = 2\pi n w_0^2/\lambda_p$ (Fig. 18). This effect enables visualization of a three-dimensional structure of complex objects [154].

In Fig. 18, we present the efficiency of third-harmonic generation as a function of the diameter D of a spherical inclusion in a medium with a third-order nonlinearity in a THG scheme with a confocal parameter $b = 7.48$ μm. As can be seen from this plot, the third-harmonic signal grows with increasing D until D reaches the confocal parameter b, and starts to decrease for $D > b$. Since third-harmonic generation is both a nonlinear and coherent process, the generation of the third harmonic is confined to a small region with a length on the order of the confocal parameter of a tightly focused driver beam. Thus, the longitudinal spatial resolution of THG microscopy is much higher than that typical of linear methods of microscopy (cf. the solid and dashed lines in Fig. 18b).

The efficiency of second-harmonic generation is governed by the second-order nonlinear-optical susceptibility $\chi^{(2)}$. A class of objects and structures that can be visualized with the aid of second-harmonic generation is determined by the symmetry of the $\chi^{(2)}$ tensor. To be visible in the second-harmonic signal, the structures need to be noncentrosymmetric [155]. Biological tissues that meet this requirement include molecular dipoles, ordered polarized structures, and noncentrosymmetric tissue domains with field-induced anisotropy. Second-harmonic generation is known to offer a powerful tool for imaging ensembles of microtubules [156]. Second-harmonic generation can also help in detecting the action potential on cell membranes stained with hyperpolarizable agents [157, 158].

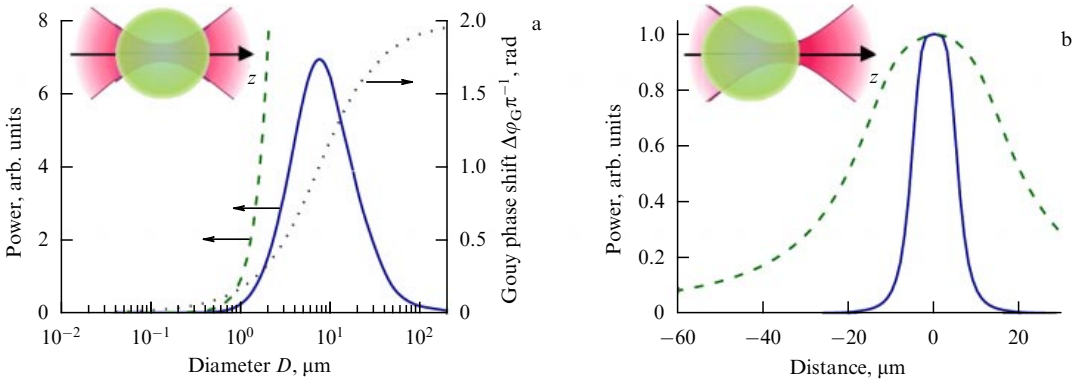

Figure 18. (a) Intensity of the third harmonic (solid line), fluorescence response (dashed line), and the Gouy phase shift $\Delta\varphi_g$ (dotted line) calculated as functions of the diameter of a spherical inclusion in a medium with third-order nonlinearity. Geometry of third-harmonic generation is sketched in the insets. The confocal parameter of the pump beam is 7.48 μm. (b) Intensity of the third harmonic (solid line) and fluorescence response (dashed line) calculated as functions of the distance between the focus and the center of the optical inclusion.

Recent experiments demonstrate that second- and third-harmonic generation microscopies can provide a subcellular resolution in the analysis of the morphological and structural properties of brain tissues in living mice [10]. A mode-locked chromium–forsterite laser system developed for the purposes of such studies [152] includes a master laser oscillator, a periodically poled nonlinear crystal with quadratic nonlinearity for highly efficient second-harmonic generation, and a photonic-crystal fiber for soliton frequency shifting. This optical system has been shown to provide a versatile platform for nonlinear microscopy of brain tissues, including those in living mice, based on second- and third-harmonic generation, as well as coherent anti-Stokes Raman scattering.

Figure 19 displays images of a 20-μm thick slice from the brain of a C57BL/6-line mouse obtained through third-harmonic generation without any staining. In this figure, we demonstrate THG images of slices from the fifth layer of the somatosensory cortex (Fig. 19a) and part of the dentate gyrus of the hippocampus (Fig. 19b). The cells are observed in these images as dark areas with a low signal intensity. The images are characterized by a high contrast and subcellular resolution, clearly visualizing morphological features of brain tissues [159].

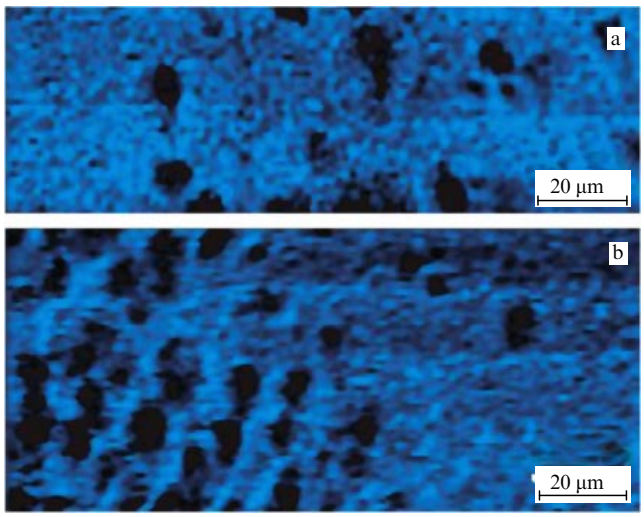

Figure 19. Stainless brain imaging in C57BL/6-line mice using third-harmonic generation: (a) the fifth layer of the somatosensory cortex, and (b) part of the dentate gyrus of the hippocampus.

Thus, optical-harmonic generation microscopy enables stainless, marker-free brain imaging with a subcellular spatial resolution. However, the miniaturization level of systems for optical-harmonic generation microscopy is not enough to apply this technology to studies of freely moving animals. The available compact microscopes allow *in vivo* second- and third-harmonic microscopy of human skin to be implemented with a penetration depth of up to 200 μm [160]. Femtosecond laser pulses needed for such studies were delivered through a large-mode-area photonic crystal fiber, supporting a single-mode guidance at 1260 nm. The backward harmonic signal was collected in this system with the aid of a multimode optical fiber. The system measured 3 cm in length.

7.2 Spontaneous Raman scattering

Methods of optical microscopy based on spontaneous Raman scattering have been in use for a long time [161–163]. The main difficulties of fiber-optic probes for Raman microscopy and Raman sensing are associated with the low signal-to-noise ratio typical of spontaneous Raman scattering. An increase in this ratio would open means for a stainless, marker-free chemically selective imaging in a broad class of systems. When experiments are performed in a fiber format, the signal of spontaneous Raman scattering needs to be detected against a strong background related to inelastic scattering from the material of the fiber [164]. One possible way to negotiate this difficulty reduces to employing a probe consisting of two fibers, where one fiber is used to deliver laser radiation, while the second probe serves to collect the Raman signal [165]. To increase the sensitivity of this method, measurements are performed with bundles consisting of a moderate number (typically no more than 20) of fibers, with the central fiber used for the delivery of laser radiation, and the other fibers providing Raman signal collection [166, 167]. Because of the large size, however, such systems are not suitable for neuroendoscopy. The search for an optimal miniature fiber probe for endoscopic brain studies is ongoing [168].

Doronina-Amitonova et al. [169] have developed a fiber-optic microprobe for Raman brain studies based on a multimode optical fiber with an outer diameter of 125 μm.

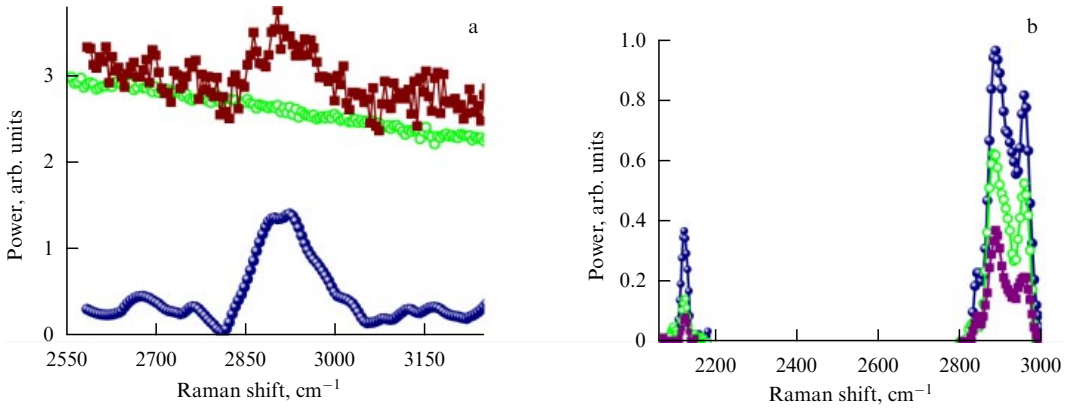

Figure 20. (a) Spectrum of Raman scattering from the brain of a C57BL/6-line mouse measured through a fiber-optic probe: (rectangles) raw spectrum, (unfilled circles) spectrum of the background from the fiber probe, and (filled circles) spectrum of Raman scattering from CH-bond vibrational mode after background subtraction. (b) The spectrum of Raman scattering from an EdU solution measured through a fiber-optic probe with an EdU concentration of 5 mM l^{-1} (rectangles), 10 mM l^{-1} (unfilled circles), and 20 mM l^{-1} (filled circles) [169].

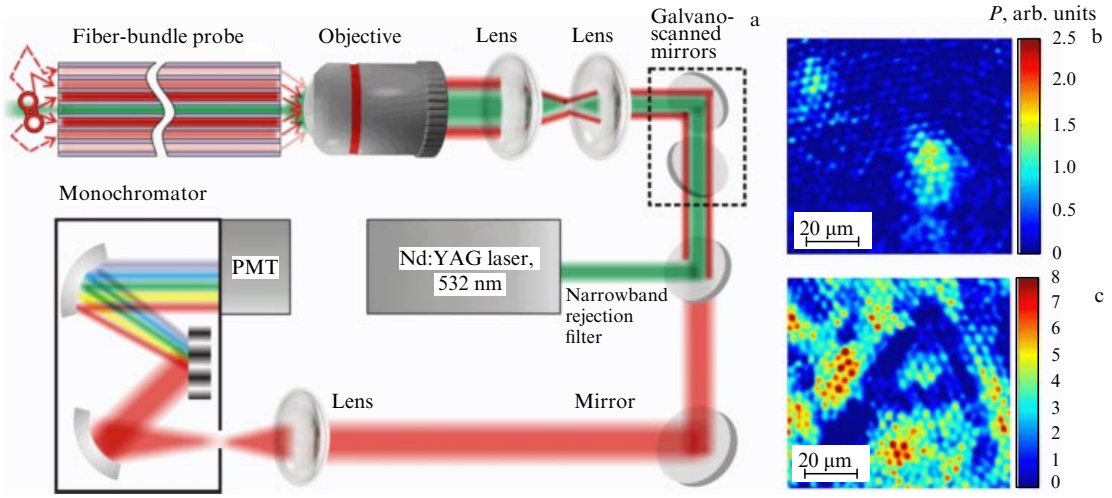

Figure 21. (a) Diagram of Raman scattering microscopy using a fiber bundle [150]. (b, c) Raman images of clusters of diamond nanoparticles on a glass substrate taken through a fiber-bundle probe after background subtraction.

This microprobe has been shown to enable the Raman sensing and Raman spectroscopy of lipids and water in a mouse brain (Fig. 20a), as well as indicators of DNA proliferation in cells widely used in neurobiology (Fig. 20b). With the appropriate spectral processing, weak signals of Raman scattering from the brain region under study can be discriminated [170] against the background of inelastic light scattering from the fiber (see Fig. 20).

Specifically designed fiber bundles can improve the sensitivity and increase the rate of fiber-optic remote detection of the Raman signal. The key idea of this approach suggests the compression of a two-dimensional image transmitted through a fiber bundle into a one-dimensional array that can be processed with a spectrometer. To this end, a large number of optical fibers (limited by the height of the charge-coupled device) are arranged into a bundle in such a way that these fibers form a circle at the input end of the fiber, and a line at the opposite end of the fiber. The output end of the fiber is then connected to a spectrometer [171–174].

For a higher sensitivity, the optical scheme processing the fiber probe output is adjusted to pick up the incoherent Raman signal simultaneously from all the fibers (about 6000) in the bundle, thus providing a large area and a high aperture of signal collection [150].

In the setup of a fiber-optic probe for Raman brain studies shown in Fig. 21a [150], a high spatial resolution is achieved thanks to the locality of the Raman response, excited by delivering the laser pump through only one 2.4-μm-in-diameter fiber in the bundle and automatically switching this laser beam between the fibers. The signal of Raman scattering passes through a system of collimated lenses and is processed by a detection system consisting of a monochromator, photomultiplier, and lock-in amplifier. The Raman images are synthesized pixel-by-pixel using the results of repeated measurements performed with each fiber in the bundle. The background subtraction is performed using the signal measured through the fiber probe off the Raman resonance. Figures 21b and 21c display images of clusters of diamond nanoparticles measured by detecting the Raman signal through the fiber-bundle probe developed.

The sensitivity of fiber-based Raman sensing and imaging can be further improved by delivering laser radiation through hollow-core fibers [111, 175–177].

7.3 Coherent Raman scattering

Methods of nonlinear optical microscopy based on coherent and stimulated Raman scattering open new avenues for the analysis of structural and chemical variations in the brain, as

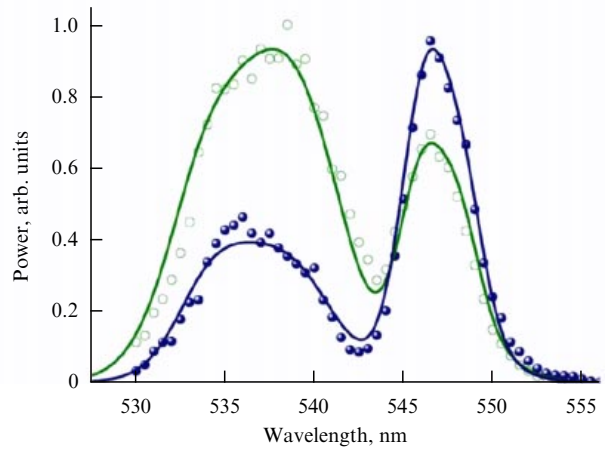

Figure 22. Typical CARS spectra measured for mouse brain regions with a high (unfilled circles) and low (filled circles) content of water [179]. Results of numerical simulations are shown by the solid lines.

well as for the stainless detection of neural activity without the need for fluorescent markers [4]. Microscopy of coherent anti-Stokes Raman scattering offers a highly sensitive chemically selective probe for brain studies in living animals [178]. High-resolution CARS images can help to visualize myelinated nerve fibers in the brains of living anesthetized animals. The myelin layer of axons features a high concentration of ordered CH_2 groups, which can be conveniently detected by CARS.

Typical CARS spectra of the cortex in a mouse brain are presented in Fig. 22. Symmetric CH modes of lipids are clearly resolved in these spectra as prominent features centered at 547 nm. The spectral features representing the symmetric and asymmetric stretching modes of water merge in these spectra, giving rise to a broad peak centered at 537 nm. The amplitude ratio of these peaks is determined by the concentration and orientation of lipids and water molecules in a brain tissue irradiated by focused laser beams [179].

Methods of CARS microscopy are widely applied for the examination of biologically significant chemical processes in the brains of living animals. These methods enable the detection of CH_2 vibrations in the brains of anesthetized animals at a rate of up to 20 frames per second [180]. Such a frame rate considerably exceeds that attainable in the microscopy of spontaneous Raman scattering. Experimental studies reveal that the spatial resolution provided by CARS microscopy is high enough to resolve fine details in the structure of nerve cells with no need for fluorescent markers or other staining agents [181, 182].

The strong background originating from the inelastic scattering of laser radiation propagating through the fiber is a cause of serious problems in CARS microscopy with fiber-optic probes. Balu et al. [183] have demonstrated a simple method for the suppression of this background using two separate fibers for the delivery of laser radiation and the Raman response — an approach similar to that employed in fiber probes for spontaneous Raman sensing.

Some of the difficulties inherent in CARS microscopy can be overcome in microscopy based on stimulated Raman scattering. In contrast to CARS, the nonlinear signal used in SRS microscopy is background-free, which gives rise to numerous advantages of SRS microscopy over its coherent counterpart. In spite of this, SRS microscopy only recently has received wide recognition as a method of chemically selective microscopy, the key limitation for a long time being related to the low frame rate (on the order of a frame per minute) at which SRS images can be obtained and the strong influence of pump attenuation in optically thick media on the SRS signal. Experimental methods developed in recent years help to address these issues [184]. In particular, the frame rate in SRS imaging can be substantially increased by tapping a modulated Stokes signal with lock-in detection of the SRS signal using specifically designed high-rate analog amplifiers [184].

In a miniature SRS microscope, demonstrated by Saar et al. [185], laser radiation is delivered through a polarization-maintaining fiber. For a field of view corresponding to 500 pixels, SRS images are accumulated in this system at a frame rate of up to 7 frames per second. Efficient SRS microscopy of skin has been demonstrated in experiments on living mice involving the 2845-cm^{-1} CH_2 vibrations in lipids, and 2950-cm^{-1} CH_3 vibrations in proteins [185].

8. Conclusion

A systematic approach to the complex problem of studying the diversity of the brain and its functions calls for innovative technologies enabling the detection of the entire set of coupled physical, chemical, and biological processes in the brain of naturally behaving mammals. Optical technologies offer unique opportunities, opening new avenues towards this goal. In the past few years, methods of optical physics have been at the heart of the efforts aimed at developing innovative technologies and unique neurointerfaces, allowing the brain of mammals and its complex functions to be studied directly in the process of their learning and cognition.

Due to their compactness and flexibility, fiber-optic neurointerfaces offer new opportunities for studying the functions of living brains in experiments with freely moving animals. Recently developed fiber-optic neurointerfaces are ideally suited for optogenetic studies, allowing the functional state of a living brain to be detected by measuring the optical response from genetically encoded fluorescent proteins. Recent experiments demonstrate the feasibility of all-optical detection of a broad class of fluorescent markers, helping to visualize functionally significant processes related to neural activity in the brain.

Nonlinear optical processes of two-photon-induced fluorescence, second- and third-harmonic generation, and nonlinear Raman scattering are finding extending applications in complex multimodal nonlinear optical microscopy, providing a wealth of information on the physical and biochemical processes accompanying higher nervous activity. Second- and third-harmonic generation, as well as nonlinear Raman scattering, enables a stainless detection of functionally significant processes in the living brain. Advanced fiber-optic technologies are being integrated with novel approaches to laser microscopy and optogenetics on an innovative compact fiber-optic platform, which enables nonlinear-optical brain imaging and includes fiber-optic laser sources, fiber frequency converters, fiber sources of supercontinuum radiation, fibers for the delivery of ultrashort laser pulses, and fiber-format ultracompact optical filters.

Acknowledgments

We are deeply grateful to M V Koval'chuk and P K Kashkarov for their constant encouragement and support of this work. We also acknowledge valuable help from, and numerous fruitful discussions with, O I Ivashkina, M A Zots, A A Lanin, A A Voronin, D A Sidorov-Biryukov, and N A Safronov.

This research was supported in part by the Russian Foundation for Basic Research (projects Nos 13-02-01465, 13-04-40335, 14-29-07182, and 14-29-07264) and the Welch Foundation (grant No. A-1801). Research described in Section 3 was supported by the federal program 'Research and Development in High-Priority Areas of Science and Technology in Russia in 2014–2020' (agreement No. 14.607.21.0092, dated 21 November 2014, unique identifier of applied research RFMEFI60714X0092). Research into microscopy using ultrashort infrared pulses was supported by the Russian Science Foundation (project No. 14-12-00772).

References

1. Lakowicz J R *Principles of Fluorescence Spectroscopy* (New York: Springer, 2006)
2. Pawley J (Ed.) *Handbook of Biological Confocal Microscopy* (New York: Springer, 2006)
3. Turrell G, Corset J (Eds) *Raman Microscopy*: *Developments and Applications* (Amsterdam: Elsevier, 1996)
4. Min W et al. *Annu. Rev. Phys. Chem.* **62** 507 (2011)
5. Evans C L, Xie X S *Annu. Rev. Anal. Chem.* **1** 883 (2008)
6. Denk W, Strickler J H, Webb W W *Science* **248** 73 (1990)
7. Hoover E E, Squier J A *Nature Photon.* **7** 93 (2013)
8. Horton N G et al. *Nature Photon.* **7** 205 (2013)
9. Débarre D et al. *Nature Meth.* **3** 47 (2006)
10. Witte S et al. *Proc. Natl. Acad. Sci. USA* **108** 5970 (2011)
11. O'Keefe J, Dostrovsky J *Brain Res.* **34** 171 (1971)
12. Hafting T et al. *Nature* **436** 801 (2005)
13. Chen L L et al. *Exp. Brain Res.* **101** 8 (1994)
14. Moser E I, Kropff E, Moser M-B *Annu. Rev. Neurosci.* **31** 69 (2008)
15. O'Keefe J, Moser M-B, Moser E I "The Nobel Prize in Physiology or Medicine 2014", Nobel Media AB 2014, Web 29 March 2015, http://www.nobelprize.org/nobel_prizes/medicine/laureates/2014/
16. Betzig E. Hell S W, Moerner W E "The Nobel Prize in Chemistry 2014", Nobel Media AB 2014, Web 29 March 2015, http://www.nobelprize.org/nobel_prizes/chemistry/laureates/2014/
17. Knöpfel T, Boyden E S (Eds) *Optogenetics*: *Tools for Controlling and Monitoring Neuronal Activity* (Progress in Brain Research, Vol. 196) (Amsterdam: Elsevier, 2012)
18. Holtmaat A et al. *Nature Protocols* **4** 1128 (2009)
19. Kerr J N D, Nimmerjahn A *Curr. Opin. Neurobiol.* **22** 45 (2012)
20. Bernstein J G. Garrity P A, Boyden E S *Curr. Opin. Neurobiol.* **22** 61 (2012)
21. Aravanis A M et al. *J. Neural Eng.* **4** S143 (2007)
22. Doronina-Amitonova L V et al. *Nature Sci. Rep.* **3** 3265 (2013)
23. Kobat D, Horton N G, Xu C *J. Biomed. Opt.* **16** 106014 (2011)
24. Flusberg B A et al. *Nature Meth.* **2** 941 (2005)
25. Fu L, Gu M *J. Microsc.* **226** 195 (2007)
26. Brecht M et al. *J. Neurosci.* **24** 9223 (2004)
27. Kerr J N D, Denk W *Nature Rev. Neurosci.* **9** 195 (2008)
28. Callaghan P T *Principles of Nuclear Magnetic Resonance Microscopy* (Oxford: Clarendon Press, 1993)
29. Schmidt K C, Smith C B *Nucl. Med. Biol.* **32** 719 (2005)
30. Cohen D *Science* **175** 664 (1972)
31. Schulz D et al. *Nature Meth.* **8** 347 (2011)
32. Gabriel M *Physiol. Behavior* **12** 145 (1974)
33. Krüger J, Bach M *Exp. Brain Res.* **41** 191 (1981)
34. Wilt B A et al. *Annu. Rev. Neurosci.* **32** 435 (2009)
35. Yang G, Pan F, Gan W-B *Nature* **462** 920 (2009)
36. Stosiek C et al. *Proc. Natl. Acad. Sci. USA* **100** 7319 (2003)
37. Tian L et al. *Nature Meth.* **6** 875 (2009)
38. Djurisic M et al. *J. Neurosci.* **24** 6703 (2004)
39. Palmer L M, Stuart G J *J. Neurosci.* **29** 6897 (2009)
40. Chalfie M et al. *Science* **263** 802 (1994)
41. Anokhin K V et al. *Brain Res.* **544** 101 (1991)
42. Boyden E S et al. *Nature Neurosci.* **8** 1263 (2005)
43. Zhang F et al. *Nature Protocols* **5** 439 (2010)
44. Zhang F et al. *Nature Meth.* **3** 785 (2006)
45. Liu X et al. *Nature* **484** 381 (2012)
46. Ji N et al. *Curr. Opin. Neurobiol.* **18** 605 (2008)
47. Shimomura O, Johnson F H, Saiga Y *J. Cell. Compar. Physiol.* **59** 223 (1962)
48. Prasher D C et al. *Gene* **111** 229 (1992)
49. Heim R, Prasher D C, Tsien R Y *Proc. Natl. Acad. Sci. USA* **91** 12501 (1994)
50. Ormö M et al. *Science* **273** 1392 (1996)
51. Cubitt A B et al. *Trends Biochem. Sci.* **20** 448 (1995)
52. Stepanenko O V et al. *Tsitologiya* **49** 395 (2007)
53. Hill D K, Keynes R D *J. Physiol.* **108** 278 (1949)
54. Bouchard M B et al. *Opt. Express* **17** 15670 (2009)
55. Malonek D, Grinvald A *Science* **272** 551 (1996)
56. Stratonnikov A A, Loschenov V B *J. Biomed. Opt.* **6** 457 (2001)
57. Helmchen F *Exp. Physiol.* **87** 737 (2002)
58. Kawata S, Ohtsu M, Irie M (Eds) *Nano-Optics* (Springer Series in Optical Sciences, Vol. 84) (Berlin: Springer, 2002)
59. Zipfel W R, Williams R M, Webb W W *Nature Biotechnol.* **21** 1369 (2003)
60. Helmchen F, Denk W *Nature Meth.* **2** 932 (2005)
61. Freudiger C W et al. *Science* **322** 1857 (2008)
62. Hell S W *Nature Meth.* **6** 24 (2009)
63. Bates M et al. *Science* **317** 1749 (2007)
64. Zheltikov A M *Phys. Usp.* **50** 705 (2007); *Usp. Fiz. Nauk* **177** 737 (2007)
65. Flusberg B A et al. *Nature Meth.* **5** 935 (2008)
66. Doronina L V et al. *Opt. Lett.* **34** 3373 (2009)
67. Snyder A W, Love J D *Optical Waveguide Theory* (London: Chapman and Hall, 1983)
68. Marcuse D *J. Opt. Soc. Am.* **68** 103 (1978)
69. Zheltikov A *J. Opt. Soc. Am. B* **22** 1100 (2005)
70. Russell P *Science* **299** 358 (2003)
71. Zheltikov A M *Phys. Usp.* **43** 1125 (2000); *Usp. Fiz. Nauk* **170** 1203 (2000)
72. Nielsen M D et al. *Opt. Lett.* **28** 2309 (2003)
73. Akimov D A et al. *Opt. Lett.* **28** 1948 (2003)
74. Foster M, Moll K, Gaeta A *Opt. Express* **12** 2880 (2004)
75. Leon-Saval S et al. *Opt. Express* **12** 2864 (2004)
76. Foster M, Gaeta A *Opt. Express* **12** 3137 (2004)
77. Salem R et al. *Nature Photon.* **2** 35 (2008)
78. Foster M A et al. *Nature* **441** 960 (2006)
79. Foster M A et al. *Nature* **456** 81 (2008)
80. Levy J S et al. *Nature Photon.* **4** 37 (2009)
81. Knight J C *Nature* **424** 847 (2003)
82. Zheltikov A M *Phys. Usp.* **47** 69 (2004); *Usp. Fiz. Nauk* **174** 73 (2004)
83. Birks T A, Knight J C, Russell P St J *Opt. Lett.* **22** 961 (1997)
84. Zheltikov A M *Optika Mikrostrukturirovannykh Volokon* (Optics of Microstructure Fibers) (Moscow: Nauka, 2004)
85. Fedotov A B et al. *Appl. Phys. B* **73** 181 (2001)
86. Zheltikov A M *Phys. Usp.* **49** 605 (2006); *Usp. Fiz. Nauk* **176** 623 (2006)
87. Fedotov A B et al. *Appl. Phys. B* **77** 313 (2003)
88. Coen S et al. *Opt. Lett.* **26** 1356 (2001)
89. Ranka J K, Windeler R S, Stentz A J *Opt. Lett.* **25** 25 (2000)
90. Jones D J et al. *Science* **288** 635 (2000)
91. Udem T, Holzwarth R, Hänsch T W *Nature* **416** 233 (2002)
92. Hartl I et al. *Opt. Lett.* **26** 608 (2001)
93. Konorov S O et al. *JETP* **99** 19 (2004); *Zh. Eksp. Teor. Fiz.* **126** 26 (2004)
94. Sidorov-Biryukov D A, Serebryannikov D A, Zheltikov A M *Opt. Lett.* **31** 2323 (2006)
95. Paulsen H N et al. *Opt. Lett.* **28** 1123 (2003)
96. von Vacano B, Wohlleben W, Motzkus M *Opt. Lett.* **31** 413 (2006)
97. Golovchenko E A et al. *JETP Lett.* **42** 87 (1985); *Pis'ma Zh. Eksp. Teor. Fiz.* **42** 74 (1985)
98. Mitschke F M, Mollenauer L F *Opt. Lett.* **11** 659 (1986)
99. Konorov S, Zheltikov A, Scalora M *Opt. Express* **13** 3454 (2005)
100. Myaing M T et al. *Opt. Lett.* **28** 1224 (2003)

101. Ye J Y et al. *Proc. SPIE* **5700** 23 (2005)
102. Fedotov I V et al. *Appl. Opt.* **48** 5274 (2009)
103. Fedotov I V et al. *Nanotechnol. Russ.* **5** 266 (2010); *Ross. Nanotekhnol.* **5** (3 – 4) 98 (2010)
104. Marcatili E A J, Schmeltzer R A *Bell Syst. Tech. J.* **43** 1783 (1964)
105. Russell P St J *J. Lightwave Technol.* **24** 4729 (2006)
106. Litchinitser N M et al. *Opt. Lett.* **27** 1592 (2002)
107. Litchinitser N M et al. *Opt. Express* **11** 1243 (2003)
108. Roberts P et al. *Opt. Express* **13** 8277 (2005)
109. Litchinitser N M, Poliakov E *Appl. Phys. B* **81** 347 (2005)
110. Zheltikov A M *Nature Mater.* **4** 267 (2005)
111. Doronina-Amitonova L V et al. *Opt. Lett.* **37** 4642 (2012)
112. Zheltikov A M *Appl. Opt.* **47** 474 (2008)
113. Zheltikov A M *Phys. Usp.* **51** 591 (2008); *Usp. Fiz. Nauk* **178** 619 (2008)
114. Doronina-Amitonova L V et al. *Appl. Phys. Lett.* **98** 253706 (2011)
115. Tauer J et al. *Laser Phys. Lett.* **4** 444 (2007)
116. Konorov S O et al. *Appl. Opt.* **43** 2251 (2004)
117. Balciunas T et al. *Nature Commun.* **6** 6117 (2015)
118. Lanin A A et al. *Appl. Phys. Lett.* **100** 101104 (2012)
119. Yaroslavsky A N et al. *Phys. Med. Biol.* **47** 2059 (2002)
120. Ishimaru A *Wave Propagation and Scattering in Random Media* (New York: Academic Press, 1978); Translated into Russian: *Rasprostranenie i Rasseyanie Voln v Sluchaino-Neodnorodnykh Sredakh* (Moscow: Mir, 1981)
121. Doronina-Amitonova L V et al. *Appl. Phys. Lett.* **101** 021114 (2012)
122. Tai D C et al. *J. Biomed. Opt.* **12** 034033 (2007)
123. Schüz A, Palm G *J. Compar. Neurol.* **286** 442 (1989)
124. Fedotov I V et al. *Appl. Phys. Lett.* **104** 083702 (2014)
125. Helmchen F et al. *Neuron* **31** 903 (2001)
126. Flusberg B A et al. *Opt. Lett.* **30** 2272 (2005)
127. Göbel W et al. *Opt. Lett.* **29** 2521 (2004)
128. Sawinski J et al. *Proc. Natl. Acad. Sci. USA* **106** 19557 (2009)
129. Engelbrecht C J et al. *Opt. Express* **16** 5556 (2008)
130. Piyawattanametha W et al. *Opt. Lett.* **34** 2309 (2009)
131. Ghosh K K et al. *Nature Meth.* **8** 871 (2011)
132. Ziv Y et al. *Nature Neurosci.* **16** 264 (2013)
133. Barretto R P J et al. *Nature Med.* **17** 223 (2011)
134. Liang C et al. *Appl. Opt.* **41** 4603 (2002)
135. Carlson K et al. *Appl. Opt.* **44** 1792 (2005)
136. Rouse A R et al. *Appl. Opt.* **43** 5763 (2004)
137. Lane P M et al. *Opt. Lett.* **25** 1780 (2000)
138. Ota T et al. *J. Biomed. Opt.* **10** 024010 (2005)
139. Kleinfeld D et al. *Proc. Natl. Acad. Sci. USA* **95** 15741 (1998)
140. Nimmerjahn A et al. *Nature Meth.* **1** 31 (2004)
141. Theer P, Hasan M T, Denk W *Opt. Lett.* **28** 1022 (2003)
142. Mittmann W et al. *Nature Neurosci.* **14** 1089 (2011)
143. Kobat D et al. *Opt. Express* **17** 13354 (2009)
144. Doronina-Amitonova L V et al. *J. Biophoton.* **3** 660 (2010)
145. Vincent P et al. *EMBO Rep.* **7** 1154 (2006)
146. Bharali D J et al. *Proc. Natl. Acad. Sci. USA* **102** 11539 (2005)
147. Davenne M et al. *Chem. Senses* **30** (Suppl. 1) i115 (2005)
148. Doronina-Amitonova L V et al. *Appl. Phys. Lett.* **101** 233702 (2012)
149. Yamaguchi S et al. *Nature* **409** 684 (2001)
150. Doronina-Amitonova L V et al. *Appl. Phys. Lett.* **102** 161113 (2013)
151. Doronina-Amitonova L V et al., in *12th Intern. Conf. on Laser Applications in Life Sciences 2010, LALS-2010, Oulu, Finland, June 9 – 11, 2010, Technical Digest*, p. 124
152. Doronina-Amitonova L V et al. *Appl. Phys. Lett.* **99** 231109 (2011)
153. Reintjes J F *Nonlinear Optical Parametric Processes in Liquids and Gases* (New York: Academic Press, 1984)
154. Squier J et al. *Opt. Express* **3** 315 (1998)
155. Campagnola P J, Loew L M *Nature Biotechnol.* **21** 1356 (2003)
156. Dombeck D A et al. *Proc. Natl. Acad. Sci. USA* **100** 7081 (2003)
157. Dombeck D A et al. *J. Neurophysiol.* **94** 3628 (2005)
158. Shneider M N, Voronin A A, Zheltikov A M *Phys. Rev. E* **81** 031926 (2010)
159. Doronina-Amitonova L V et al. *Appl. Phys. Lett.* **103** 093701 (2013)
160. Chia S-H et al. *Opt. Express* **18** 17382 (2010)
161. Mizuno A et al. *J. Raman Spectrosc.* **25** 25 (1994)
162. Koljenović S et al. *J. Biomed. Opt.* **10** 031116 (2005)
163. Krafft C et al. *Anal. Bioanal. Chem.* **389** 1133 (2007)
164. Udovich J A et al. *Appl. Opt.* **47** 4560 (2008)
165. McCreery R L, Fleischmann M, Hendra P *Anal. Chem.* **55** 146 (1983)
166. Bergholt M S et al. *J. Biophotonics* **6** 49 (2013)
167. Krafft C et al. *Biomed. Spectrosc. Imaging* **1** 39 (2012)
168. Komachi Y et al. *Appl. Opt.* **48** 1683 (2009)
169. Doronina-Amitonova L V et al. *Appl. Phys. Lett.* **101** 113701 (2012)
170. Beier B D, Berger A J *Analyst* **134** 1198 (2009)
171. Ma J, Ben-Amotz D *Appl. Spectrosc.* **51** 1845 (1997)
172. Gift A D et al. *J. Raman Spectrosc.* **30** 757 (1999)
173. McClain B L, Jiaying, Ben-Amotz D *Appl. Spectrosc.* **53** 1118 (1999)
174. Dochow S et al. *Opt. Express* **20** 20156 (2012)
175. Komachi Y et al. *Opt. Lett.* **30** 2942 (2005)
176. Sato H et al. *Vibration. Spectrosc.* **50** 125 (2009)
177. Konorov S O et al. *Opt. Lett.* **31** 1911 (2006)
178. Evans C L et al. *Opt. Express* **15** 12076 (2007)
179. Voronin A A et al. *Opt. Lett.* **36** 508 (2011)
180. Evans C L et al. *Proc. Natl. Acad. Sci. USA* **102** 16807 (2005)
181. Fu Y et al. *Opt. Express* **16** 19396 (2008)
182. Légaré F et al. *Opt Express* **14** 4427 (2006)
183. Balu M et al. *Opt. Express* **18** 2380 (2010)
184. Saar B G et al. *Science* **330** 1368 (2010)
185. Saar B G et al. *Opt. Lett.* **36** 2396 (2011)